Journal of
Materials Chemistry C

ROYAL SOCIETY
OF CHEMISTRY

REVIEW

View Article Online
View Journal | View Issue

Cite this: *J. Mater. Chem. C*, 2024, **12**, 15276

Organic and inorganic semiconducting materials-based SERS: recent developments and future prospects

Resul Ozdemir,[a] Kubra Ozkan Hukum,[b] Hakan Usta *[c] and Gokhan Demirel *[b]

Received 9th June 2024,
Accepted 10th September 2024

DOI: 10.1039/d4tc02391a

rsc.li/materials-c

Surface-enhanced Raman spectroscopy (SERS) with high sensitivity/selectivity is a powerful analytical tool and has been widely used, particularly in the fields of chemistry, spectroscopy, molecular detection, food safety, anti-counterfeiting, and environmental monitoring. Conventional SERS detection relies on plasmonic materials (*e.g.*, Au and Ag nanostructures) with exceedingly high enhancement factors up to 10^{12}. However, these substrates encounter significant limitations, including poor reproducibility, high cost, lack of selectivity, limited SERS active area leading to inconsistent field enhancement and SERS signals, and the possibility of the photothermal decomposition of the analyte species. These drawbacks have the potential to impede detection accuracy and hinder large-scale practical applications. This review focuses on alternative approaches based on noble metal-free SERS substrates. Considering recent advancements in the field of SERS active platforms, we first introduce the implementation of inorganic compounds, including metal oxides, transition metal sulfides/-selenides/-tellurides, 2-D layered transition metal carbides and nitrides (Mxenes), metal–organic frameworks (MOFs), and single elemental inorganic materials for Raman signal enhancement applications. In the second part of the review, we highlight the fast-growing field of SERS-active organic platforms. Moreover, we discuss the promises and challenges for the future direction of organic and inorganic material-based SERS.

1. Introduction

Surface-enhanced Raman spectroscopy (SERS) is of great interest in ultrasensitive molecular detection, especially in the fields of sensing, catalysis, molecular tracking, and anti-counterfeiting.[1–9] Since the discovery of SERS by Fleischmann *et al.*,[10] noble metals in the form of nanostructures or nanoparticles have conventionally been employed as SERS-active platforms due to their strong electromagnetic enhancement contributions through the excitation of surface-plasmon polaritons upon the interaction of a laser source with a suitable wavelength.[11–14] Significant developments and discoveries in the fabrication of noble metal nanoparticles with varying shapes and unique surface-plasmon resonance features, as well as plasmonic platforms with 3-dimensional (3-D) nano-/micro-morphologies, have been achieved to date.[15,16] Since many comprehensive review articles have already covered in-depth discussions of the enhancement mechanism in SERS based on noble metals, a detailed attempt has not been made here.[1–5,17,18] Despite the advantages of noble metal substrates in SERS applications, they confront rigorous challenges, including poor reproducibility, high cost, lack of selectivity, limited SERS active area leading to inconsistent field enhancement and SERS signals, and the possibility of the photothermal decomposition of the analyte species. Therefore, the discovery of non-plasmonic platforms is certainly needed to broaden the applicability of SERS and further study fundamental phenomena. To this end, organic and inorganic compounds with unique surface properties, high chemical stabilities, structural diversities, and controllable optoelectrical features have risen to prominence as active materials in the field of SERS.[19–24] This review provides an overview on the recent advances in the development and applications of SERS-active organic/inorganic material platforms. To this end, we first summarize the plausible chemical enhancement mechanisms and then introduce the development of SERS-active inorganic materials in the second part, including metal oxides, transition metal sulfides/-selenides/-tellurides, Mxenes, metal–organic frameworks (MOFs), and single elemental inorganic materials. In the third part, we present recent advances in organic material-based SERS platforms and finally outline promises and challenges

---

[a] Department of Electronics and Automation, Eskişehir Vocational School, Eskişehir Osmangazi University, 26110 Eskişehir, Türkiye

[b] Bio-inspired Materials Research Laboratory (BIMREL), Department of Chemistry, Gazi University, 06500 Ankara, Türkiye. E-mail: nanobiotechnology@gmail.com

[c] Department of Materials Science and Nanotechnology Engineering, Abdullah Gül University, 38080 Kayseri, Türkiye. E-mail: hakan.usta@agu.edu.tr

for the future direction of organic and inorganic material-based SERS.

Yamada, Yamamoto, and Tani, in 1982, for the first time, identified significant Raman signal enhancement from pyridine molecules upon adsorption onto NiO.[25] To explain this observation, Yamada and Yamamoto, in 1983, investigated the Raman signal enhancement of chemisorbed pyridine on different types of inorganic semiconductors (*i.e.*, Ni, Ti, and Co).[26] They demonstrated that the observed Raman signal enhancements are based on the charge-transfer excitation of the absorbent–adsorbate interactions. It is obvious that charge-/energy-transfer processes between the molecule and SERS substrate systems play a vital role in the Raman signal enhancements for noble metal-free platforms. Under electromagnetic radiation, numerous energetically and thermodynamically possible charge-/energy transfer (CT) pathways between the molecular species and (in)organic surfaces can take place, as proposed by Lombardi and Birke.[21] Among them, the CT

Resul Ozdemir

Resul Ozdemir received his BS degree in Chemistry from Ankara University (Turkiye) in 2008. He obtained both his MS and PhD degrees from Abdullah Gül University under the supervision of Prof. Hakan Usta in 2016 and 2021, respectively. Following this, he joined the PCN research group in the Department of Chemistry at Gent University, where he worked as a post-doctoral researcher under the guidance of Prof. Zeger Hens from 2021 to 2022. He is currently an Assistant Professor in the Department of Electronics and Automation at Eskişehir Osmangazi University. His research is mainly focused on the synthesis of novel molecular/polymeric π-conjugated materials and their integration into optoelectronic devices, such as thin-film transistors and photovoltaics.

Kubra Ozkan Hukum

Kübra Ozkan Hukum received her BS degree in Chemistry and Chemical Engineering from Gazi University (Ankara, Türkiye) in 2013 and 2014, respectively. She obtained her MSc. and PhD degrees in Chemistry in 2018 and 2023, respectively. She is currently working as an Assistant Professor at Gazi University. Her research is mainly focused on the smart polymers, surface modification, soft robotics, and surface-enhanced Raman spectroscopy.

Hakan Usta

Hakan Usta obtained his PhD degree in Chemistry from Northwestern University (IL, USA) in 2008. He then joined Polyera Corporation (IL, USA), where he held Senior Research Scientist and Project Leader positions between 2008 and 2013. He then joined the faculty at Abdullah Gül University (Kayseri, Turkiye), where he is currently a full Professor in the Department of Materials Science and Nanotechnology Engineering. Dr Usta was the recipient of Young Investigator Awards from the Turkish Academy of Sciences (TÜBA, 2015) and The Scientific and Technological Research Council of Turkey (TÜBİTAK, 2020). Dr Usta has published more than 80 research articles, 3 book chapters, and holds 16 international patents. His current research interests include the development of novel π-systems, organic (opto)electronic materials and devices, micro-/nano-structured organic films, organic-SERS, and organic-PUFs.

Gokhan Demirel

Gokhan Demirel earned his BS degree in Chemistry from Gazi University (Ankara, Türkiye) in 2000. He received his MSc and PhD degrees in the same department in 2003 and 2006. After completing his PhD degree, he became a postdoctoral researcher in the bioengineering division at Hacettepe University (Turkiye) from 2006 to 2007. Later, he worked as a postdoctoral fellow at University College Cork (Ireland) and Pennsylvania State University (US) from 2007 to 2010. He is currently a full Professor at Gazi University. He has published more than 100 research articles, and his research interests include bio-inspired materials, soft-robotics, functional thin films, and their applications.

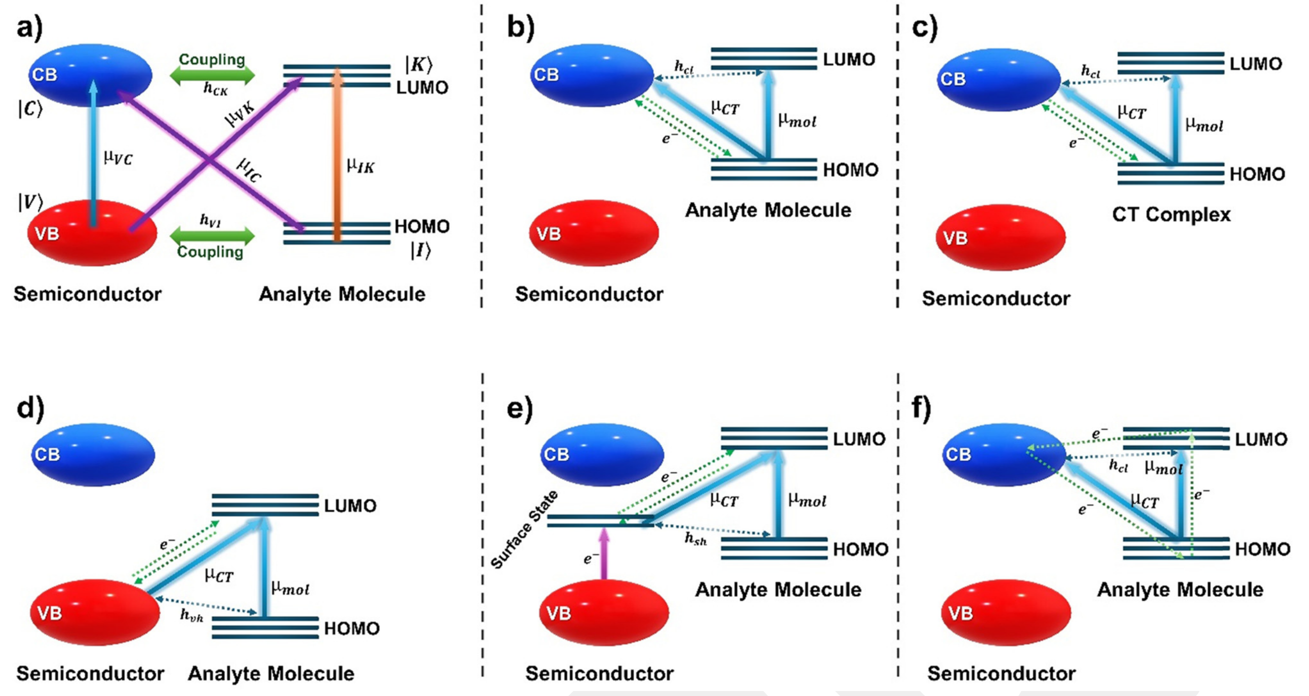

Fig. 1 Charge transfer (CT) transitions in the molecule's (in)organic SERS-active compound (named a semiconductor here) system (a). Possible CT paths in the semiconductor/molecule systems: (b) from the molecule's HOMO to the semiconductor's CB, (c) from the CT complex to the semiconductor's CB, (d) from the semiconductor's VB to the molecule's LUMO, (e) from the surface state to the molecule's LUMO, and (f) from the semiconductor's CB to the molecule's HOMO.

from a molecule to an (in)organic SERS-active compound or *vice versa*, which occurs due to the vibronic coupling within them, is called photo-induced charge-transfer (PICT) and serves as the main process in Raman signal enhancement. To understand the contribution of vibronic coupling in these systems in detail, various theoretical and experimental studies have recently been carried out.[27–31] These comprehensive approaches have led to the determination of the molecular polarizability tensor, which aligns with the predictions of Herzberg–Teller theory and provides a detailed description of the complex coupling interaction.[32] The CT complex forms at the interface when molecules are in the close vicinity of the inorganic compounds. If the energy levels of the molecule and the SERS-active compound align well, this CT complex can significantly enhance Raman signals at the excitation frequencies that resonate with the PICT transition. As illustrated in Fig. 1a, the PICT transitions occur either from the valence band (VB) of the (in)organic SERS-active compound to the molecule excited states or from the molecule ground states to the conduction band (CB) of the (in)organic SERS-active compound through a transition dipole moment μ_{IC} or μ_{VK}, respectively. As a result, intramolecular transitions (μ_{IK}) or exciton transitions (μ_{VC}), depending on the coupling, enhance the CT intensity. Possible CT pathways, including molecule HOMO-to-CB, CT complex-to-CB, VB-to-molecule LUMO, surface state-to-molecule LUMO, and CB-to-molecule HOMO, based on thermodynamically permissible transitions and the alignment of energy levels between the molecule and the (in)organic SERS-active compound, are demonstrated in Fig. 1b–f. In the first mechanism, incident light excites the electron from the molecule's HOMO to an energy level of the CB in the (in)organic SERS-active compound. This excited electron then immediately returns to a certain ground state energy level of the analyte molecule and releases a Raman photon (Fig. 1b). In the second possible mechanism, a charge transfer (CT) complex forms between the (in)organic SERS-active compound and the analyte molecule. The formation of such a complex leads to an enhancement in the polarizability of the molecules (Fig. 1c). Another CT pathway occurs between the valence band of the (in)organic SERS-active compound and the molecule's LUMO level, releasing a Raman photon (Fig. 1d). The CT process is also possible by exciting an electron in the (in)organic SERS-active compound's valence band to a defect on the surface, creating a localized surface state. This electron in the surface state can be further excited to the adsorbed molecule's lowest unoccupied molecular orbital (LUMO). This final transition back down from the LUMO to the surface state releases a Raman photon, as depicted in Fig. 1e. If the excitation energy of light aligns with the energy level of the analyte molecules, the electron is first excited from the molecule's HOMO to the LUMO level. The excited electron on the molecule's LUMO can then tunnel directly into the (in)organic SERS-active compound's conduction band. Finally, the electron relaxes back to its ground state in the molecule, releasing a detectable Raman photon (Fig. 1f).

2. Inorganic semiconductor-based SERS platforms

Since the first discovery in the 1980s,[25,26] inorganic semiconductor materials have stimulated extensive research in the field of SERS. To this end, numerous metal oxides, transition metal sulfides/-selenides/-tellurides, 2-D layered transition metal carbides and nitrides (Mxenes), metal–organic frameworks (MOFs), and even single elemental inorganic semiconductors have been proposed to be SERS active materials (Fig. 2). Table 1 summarizes the inorganic semiconductor-based SERS active platforms. Among all the inorganic semiconductors investigated to date, metal oxides have been widely investigated as an active platform for SERS investigation because they are durable, easy to make, and affordable.[33–35] Many metal oxides, such as titanium dioxide (TiO_2),[31] zinc oxide (ZnO),[36] cuprous oxide (Cu_2O),[37] molybdenum oxides (MoO_x),[38] tungsten oxides (WO_{3-x}),[39] vanadium oxides (particularly V_2O_5, VO_2, and V_2O_3),[40,41] and silver oxide (Ag_2O),[42] have been proven to display SERS activity. For example, in 2009, Musumeci *et al.* evaluated the Raman scattering of dopamine and dopac (3,4-dihydroxy-phenylacetic acid) molecules adsorbed on the TiO_2 nanostructures.[43] Depending on the size and shape of the synthesized TiO_2 structures, they observed a Raman signal enhancement of up to $\sim 10^3$ for the TiO_2/molecule systems. In the same work, the researchers also found that not all vibrational modes of the molecules are enhanced equally. This selectivity suggests that the molecules interact and orient themselves uniquely on the TiO_2 surface, leading to a ''molecular specificity'' in the SERS enhancement and the possibility for high-sensitivity detection of the biomolecules. In another work, Qi *et al.* demonstrated a sensitive SERS detection for a model methylene blue (MB) molecule up to 10^{-6} M using plasmon-free TiO_2 inverse opal platforms.[44] They reported that the observed selectivity for the analyte molecules is due to the position of the photonic band gap in the platforms. More recently, Ji and co-workers fabricated amorphous and anatase TiO_2 particles with submicron sizes to investigate the Raman signal enhancement performance of inorganic semiconductor platforms.[45] The experimental and theoretical calculations show that the observed enhancement is mainly due to the Mie resonances induced by a unique submicrometer spherical structure of TiO_2. The researchers also identified the anchoring mechanism of the analyte molecules (*i.e.*, *p*-mercaptobenzoic acid) with the SERS active TiO_2 surface, which highly depends on the exposure of different acid sites on the inorganic semiconductor surfaces. For inorganic semiconductors, the interplay between the surface states of the substrate material and its interaction with the analyte molecule is an crucial aspect of the SERS effect.

One promising approach for controlling the surface states of semiconducting materials for SERS applications involves adjusting their oxygen deficiency, as demonstrated by Zhao and co-workers.[31] In this work, vacancy-containing sea urchin-like $W_{18}O_{49}$ nanowires were fabricated by a hydrothermal reaction starting from WCl_6. When the fabricated $W_{18}O_{49}$ platforms were compared with a defect-free WO_3 substrate, which provides extremely weak Raman signal enhancements, they observed that the resulting platforms demonstrate a limit of detection value as low as 10^{-7} M and a Raman signal enhancement of up to 1.9×10^5, which is comparable to noble metals. To understand the importance of oxygen vacancies in SERS, the researchers further introduced vacancies in the $W_{18}O_{49}$ material by annealing them in an Ar or H_2 atmosphere. This

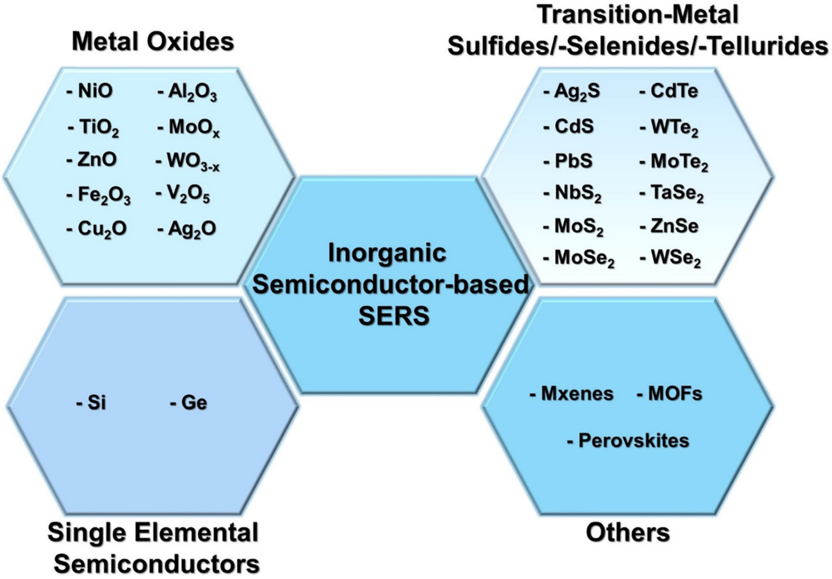

Fig. 2 Summary of the inorganic semiconductor-based SERS platforms divided into metal oxides (NiO,[25] TiO_2,[46,47] ZnO,[48] Fe_2O_3,[49] Cu_2O,[50] Al_2O_3, MoO_x,[38] WO_{3-x},[51] V_2O_5,[41] and Ag_2O[42]), transition metal sulfides/-selenides/-tellurides (Ag_2S, CdS, PbS, NbS_2,[52] MoS_2,[53] CdTe,[54] WTe_2,[55] $MoTe_2$,[55] ZnSe,[56] $TaSe_2$, WSe_2, and $MoSe_2$[57]), single elemental semiconductors (Si[58] and Ge[58]), and others (Mxenes,[59] MOFs,[60] and perovskites[61]) that are discussed in this review.

Table 1 Comparison of SERS-active inorganic semiconductor materials

Substrate	Analyte molecule	Detection limit (M)	Enhancement factor (EF)	Ref.
Metal oxides				
2D amorphous TiO_2 nanosheets	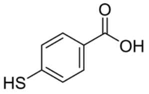 4-mercaptobenzoic acid (**4-MBA**)	10^{-4}	1.9×10^{6}	62
MoO_2 nanosheets	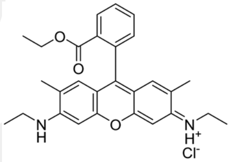 Rhodamine 6G (**R6G**)	10^{-8}	2.1×10^{5}	63
$HXMoO_3$	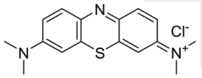 Methylene Blue (**MB**)	10^{-9}	9.5×10^{5}	64
TiO_2	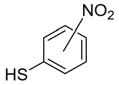 Nitrothiophenol isomers (o,m,p-**NTP**)	—	10^{2}–10^{3}	46
TiO_2	MB	10^{-10}	2.2×10^{6}	47
$SnS_2/SiO_2/Si$	SARS-CoV-2S protein	10^{-16}	—	65
TiO_2	4-MBA	10^{-6}	4.6×10^{6}	66
In_2O_3	4-MBA	—	1.2×10^{4}	67
Zn–ZrO_2	4-MBA	—	1.9×10^{4}	68
Urchin-like $W_{18}O_{49}$	R6G	10^{-7}	3.4×10^{5}	31
Mo-doped Ta_2O_5	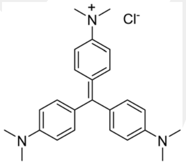 Methyl violet (**MV**)	10^{-9}	2.2×10^{7}	69
MoO_3 v-QDs	R6G	10^{-9}	10^{6}	70
MoO_3 x@MoO_3 nanosheets	MB	10^{-7}	1.4×10^{5}	71
TiO_2 photonic artificial microarrays	MB	10^{-6}	2.0×10^{4}	44
WO_{3-x} films	R6G	10^{-8}	1.1×10^{4}	51
α-MoO_{3-x} nanobelts	R6G	10^{-8}	1.8×10^{7}	34
Cu_2O cube-like superstructures	R6G	10^{-9}	8×10^{5}	50
Amorphous ZnO nanocages	4-MBA	10^{-4}	6.6×10^{5}	48

Table 1 (*continued*)

Substrate	Analyte molecule	Detection limit (M)	Enhancement factor (EF)	Ref.
Metal oxides				
Metallic MoO_2	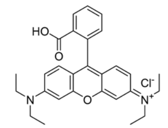 Rhodamine B(**RhB**) 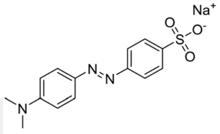 Methyl Orange (**MO**) 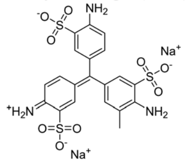 Fuchsin acid (**FA**)	10^{-7}	3.7×10^{6}	38
Indium-tin-oxide (ITO)	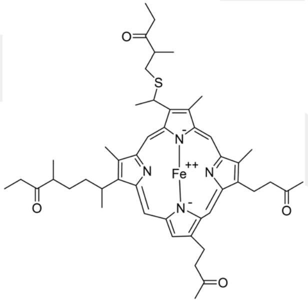 Cytochrome c	10^{-6}	500	72
α-Fe_2O_3 snowflakes/Ag	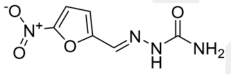 Antibiotic nitrofurazone	10^{-14}	3.0×10^{12}	49
Ni-TiO_2 IOPM	4-MBA	10^{-11}	—	73
GO/ZnO platforms	R6G	10^{-10}	7×10^{4}	74
GO/ZrO_2	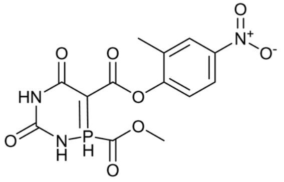 Methyl parathion (**MP**)	10^{-7}	8.8×10^{4}	75

Table 1 (*continued*)

Substrate	Analyte molecule	Detection limit (M)	Enhancement factor (EF)	Ref.
Metal oxides				
Transition-metal sulfides/-selenides/-tellurides				
F_4TCNQ/MoS_2 nanocomposites	MB	10^{-10}	2.5×10^6	76
CdTe quantum dots	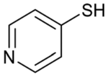 4-Mercaptopyridine (**4-MPY**)	—	10^4	54
$MoTe_2$ films	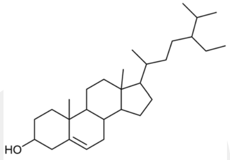 β-sitosterol	—	10^4	77
ZnSe nanowires	R6G and MB	10^{-11}	6.9×10^7	56
CuS thin films (1 nm)	R6G	10^{-12}	7.2×10^4	78
Oxygen incorporation in MoS_2	R6G	10^{-7}	10^5	30
1T-MoSSe films	R6G	10^{-7}	6×10^6	57
2H-MoS_2 monolayers	R6G	10^{-8}	4.5×10^6	79
Pt/Vertically aligned-MoS_2/TiO_2 nanotube arrays	R6G	10^{-6}	2.1×10^5	80
Rhodium sulfide (Rh_3S_6)	R6G	10^{-7}	10^5	81
c@a-CdTe	4-MBA	—	8.8×10^5	82
2D $PtTe_2$	R6G, RhB, and CV	10^{-10}	—	83
ReS_2 nanosheets	R6G and MB	10^{-9}	—	84
GaSe	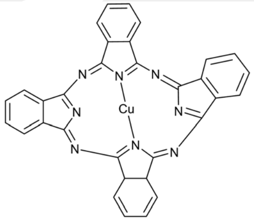 Copper phthalocyanine (**CuPc**)	—	14	85
1T'-W(Mo)Te_2	R6G	10^{-15}	10^9	55
NbS_2	MB	10^{-14}	1.1×10^3	52
TiS_2	R6G	10^{-8}	3.2×10^5	86
CdSe	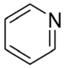	—	10^5	87
MoS_2	(5′-3′) UAA CAC UGU CUG GUA AAG AUG G MicroRNA	10^{-15}	—	53
Single elemental semiconductors				
Graphene		10^{-8}	2–17	88

Table 1 (*continued*)

Substrate	Analyte molecule	Detection limit (M)	Enhancement factor (EF)	Ref.
Metal oxides				
Si nanowire	**R6G** 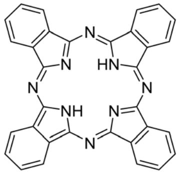 Phthalocyanine (**Pc**) 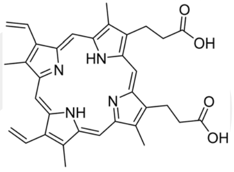 Protoporphyrin IX (**PPP**) 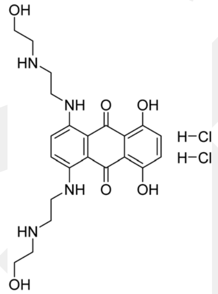 Mitoxantrone	10^{-5}	10^3	89
Graphene	RhB	10^{-11}	—	90
3D/2D-graphene/Ge	RhB	10^{-10}	—	91
Ge	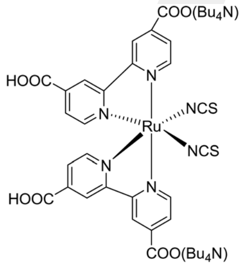 (Bu4N)2[Ru(dcbpyH)2-(NCS)2] (**N719**)	—	10^2	58
Si	R6G	—	10^2	
Boron-doped diamond (BDD)	MB	10^{-7}	10^4–10^5	92
Others				
Fe_3O_4@MOF (Co)	RhB	10^{-8}	10^8	93

Table 1 *(continued)*

Substrate	Analyte molecule	Detection limit (M)	Enhancement factor (EF)	Ref.
Metal oxides				
Co-TCPP MOFs	R6G	10^{-6}	2.7×10^4	60
Zeolitic imidazolates framework-67 (ZIF-67)	MB	10^{-8}	6.1×10^6	94
ZIF-67	R6G	10^{-7}	1.9×10^6	60
$Cu_2O@SiO_2@ZIF-8@Ag$	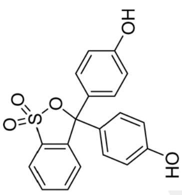 Phenol red	—	1.7×10^7	95
Ti_3C_2TX (MXene)	R6G	10^{-7}	10^6	59
Ti_3C_2TX (MXene) nanosheet	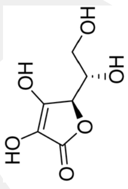 L-ascorbic acid	10^{-7}	10^7	96
Ti_2NTx (MXene)	R6G	—	10^{12}	97
InAs/GaAs QDs	pyridine	—	10^3	98

treatment resulted in an even stronger Raman signal enhancement with an EF of 3.4×10^5. In a recent work by Li *et al.*,[65] a SERS platform with Fabry–Pèrot cavities was fabricated by depositing ultrathin tungsten metal, tungsten oxide (WO_3), and oxygen-deficient tungsten oxide (WO_{3-x}) layers on polyethylene terephthalate (PET) films using a DC magnetron sputtering system (Fig. 3). The authors demonstrated that the absorption maxima of the fabricated $WO_{3-x}/WO_3/W$ platforms were precisely modulated by controlling the intermediate WO_3 layer thickness because Fabry–Pèrot (F–P) cavities into semiconductors provide flexibility in controlling the optical absorption maximum of the substrates. To this end, to obtain maximum absorption at 532 or 633 nm, or at neither of these wavelengths, they designed three different platforms with a fixed thickness of W ($\sim$7 nm) and WO_{3-x} ($\sim$100 nm) but a varying thickness of WO_3 as 168 (R-WO/W), 215 (G-WO/W), and 110 nm (Y-WO/W). By leveraging the interference effect, the researchers achieved significant differences in light absorption at specific wavelengths (532 nm and 633 nm) for each fabricated film. The R-WO/W film showed very high absorption ($\sim$99%) at 532 nm and lower absorption ($\sim$68%) at 633 nm. Conversely, the G-WO/W film displayed high absorption ($\sim$94%) at 633 nm and lower absorption ($\sim$51%) at 532 nm. The Y-WO/W film, designed as a control, had relatively low absorption at both wavelengths ($\sim$48% at 532 nm and $\sim$51% at 633 nm). Afterward, the Raman signal enhancement performances of the platforms were evaluated using methylene blue (MB) and rhodamine 6G (R6G) as Raman reporters under excitation wavelengths of 532 and 633 nm. For the 532 nm laser wavelength, the R-WO/W film significantly outperformed the G-WO/W and Y-WO/W ones in terms of the Raman signal enhancement for the R6G analyte molecule. The researchers also tested the fabricated platforms with another Raman reporter molecule, MB, at a concentration of 10^{-5} M using a laser wavelength of 633 nm. They found that the G-WO/W film provided the strongest Raman signal enhancement performance for MB compared to R-WO/W and Y-WO/W films. Notably, this is the opposite trend compared to the results obtained with the R6G molecule under the 532 nm laser excitation. These findings clearly highlight the color-dependent nature of the SERS enhancement in these substrates. The specific color depends on the reporter molecule being detected and the laser wavelength used. Additionally, all the colored F–P type substrates (red, green, and yellow) displayed stronger SERS signals than reference transparent WO_{3-x}/PET substrates. This confirms that the F–P cavity structure itself contributes to further signal enhancement, regardless of the specific color. Furthermore, as a proof of concept, the authors have demonstrated a rather low detection limit of 10^{-16} M for the SARS-CoV-2S protein using fabricated platforms.

In addition to SERS investigations of semiconductor metal oxides, transition metal chalcogenides (TMX, where X = sulfur (S), selenium (Se), or tellurium (Te)) offer a unique combination of properties and, therefore, have emerged as promising candidates for SERS applications.[77,99,100] TMX materials possess a

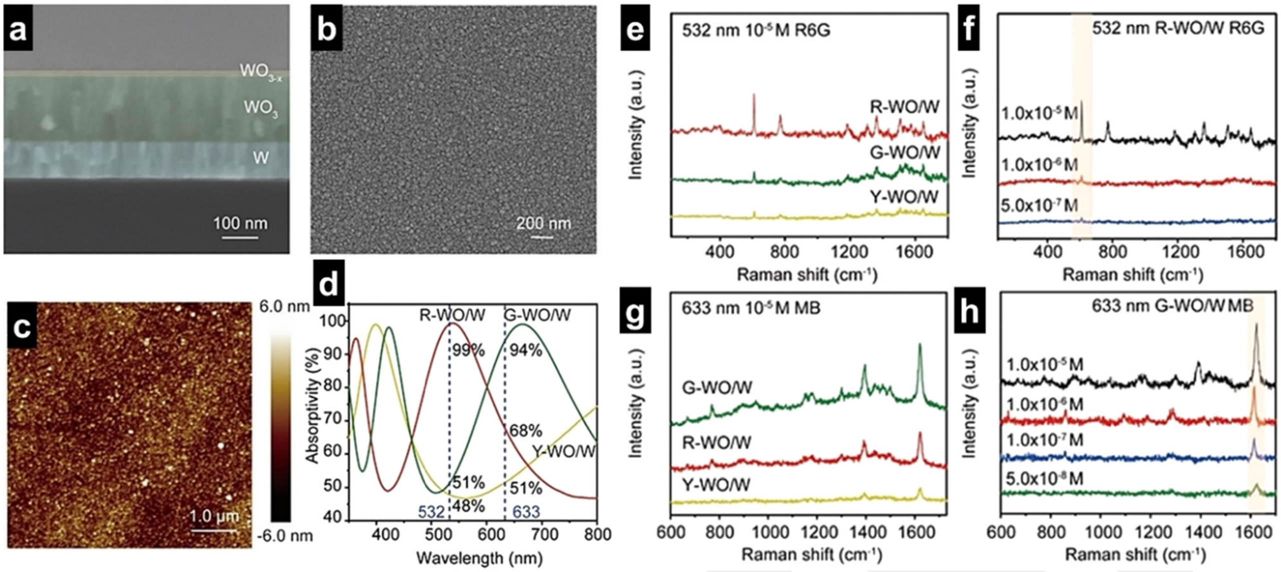

Fig. 3 SEM (cross-sectional (a) and top-view (b)) and AFM (c) images of the fabricated $WO_{3-x}/WO_3/W$ platforms. (d) Optical percent absorptivity spectra of R-WO/W, G-WO/W, and Y-WO/W platforms. SERS spectra of the R6G analyte molecule on the R-WO/W, G-WO/W, and Y-WO/O under a laser excitation of 532 nm (e). SERS spectra of R6G at different concentrations on an R-WO/W platform (f). SERS spectra of the MB probe molecule on the G-WO/W, R-WO/W, and Y-WO/O under a laser excitation of 633 nm (g). SERS spectra of MB at different concentrations on the G-WO/W platform (h).[65] Reprinted with permission from ref. 65 Copyright 2023, Wiley-VCH.

wide range of electronic and structural properties that can be tailored to achieve optimal SERS performance.[52,101] This allows researchers to design substrates specifically suited for detecting different types of analyte molecules. For example, Kim *et al.* have recently reported on an ultrathin covellite copper sulfide (CuS) film as an effective SERS platform.[78] They fabricated CuS platforms by simply sulfurizing a Cu thin film at room temperature. The SERS performance of the films was evaluated using R6G analyte molecules. Under 532 nm laser excitation, the fabricated CuS films demonstrate ∼40 times higher Raman signal enhancement than that of Cu_2O platforms. The authors suggest that two key factors of the ultrathin CuS substrate contribute to the stronger Raman signals. The presence of polar covalent bonds between copper (Cu) and sulfur (S) atoms in CuS and the strong interactions between the individual layers within the ultrathin CuS film leads to an increase in the probability of charge transfers between the R6G analyte molecules and the CuS film. In another work, Tao *et al.* reported that chemical vapor deposition (CVD)-based fabricated 1T′-WTe_2 and 1T′-$MoTe_2$ demonstrate strong Raman signal enhancement performance for analyte R6G molecules.[55] Based on experimental and theoretical investigations, the researchers suggest the underlying Raman signal enhancement mechanisms through effective charge transfer transitions from the analyte HOMO level to the telluride Fermi level and from the telluride Fermi level to the analyte LUMO level. Rani *et al.* also reported a film of MoSSe with 1T phase for SERS applications (Fig. 4).[57] The transition metal dichalcogenide materials used in this work were fabricated *via* a high-temperature and solid-state synthesis method. The Langmuir–Blodgett (LB) technique was also employed to deposit fabricated chalcogenide films. Comparing the symmetric analogs ($MoS_2/MoSe_2$), they observed that MoSSe films demonstrate about 9-fold higher enhancement in Raman intensity for the model R6G molecule. The underlying enhancement mechanism for the system under investigation was analyzed using density functional theory (DFT) calculations and showed a small energy difference between the HOMO of R6G and the Fermi level of MoSSe monolayers as compared to MoS_2 and $MoSe_2$, resulting in strong coupling of MoSSe with the analyte R6G.

Single-element semiconductors (*i.e.*, Si and Ge), with their unique electronic and structural properties, have emerged as promising candidates for next-generation SERS platforms, offering the potential for highly sensitive and versatile detection of molecules. In a study by Wang *et al.* (2011),[58] silicon (Si) and germanium (Ge) nanostructures were investigated for their ability to enhance Raman signals. The researchers found that treating these nanostructures with hydrofluoric acid created a surface rich in hydrogen atoms. These hydrogen atoms act as beneficial binding sites for the molecules being detected (analytes). Moreover, the presence of hydrogen atoms improved the transfer of electrons between the nanostructure and the analyte molecules. This enhanced electron transfer resulted in a significant signal boost for various molecules.

In addition to the above-mentioned class of inorganic semiconductor platforms, the development of noble metal-free SERS platforms has recently focused on more complex architectures by combining inorganic materials such as 2-D layered transition metal carbides and nitrides known as MXenes, metal–organic frameworks (MOFs), and perovskites. For the first time, in 2017, Gogotsi and co-workers demonstrated that 2-D titanium carbide Mxene, $Ti_3C_2T_x$, enhances the

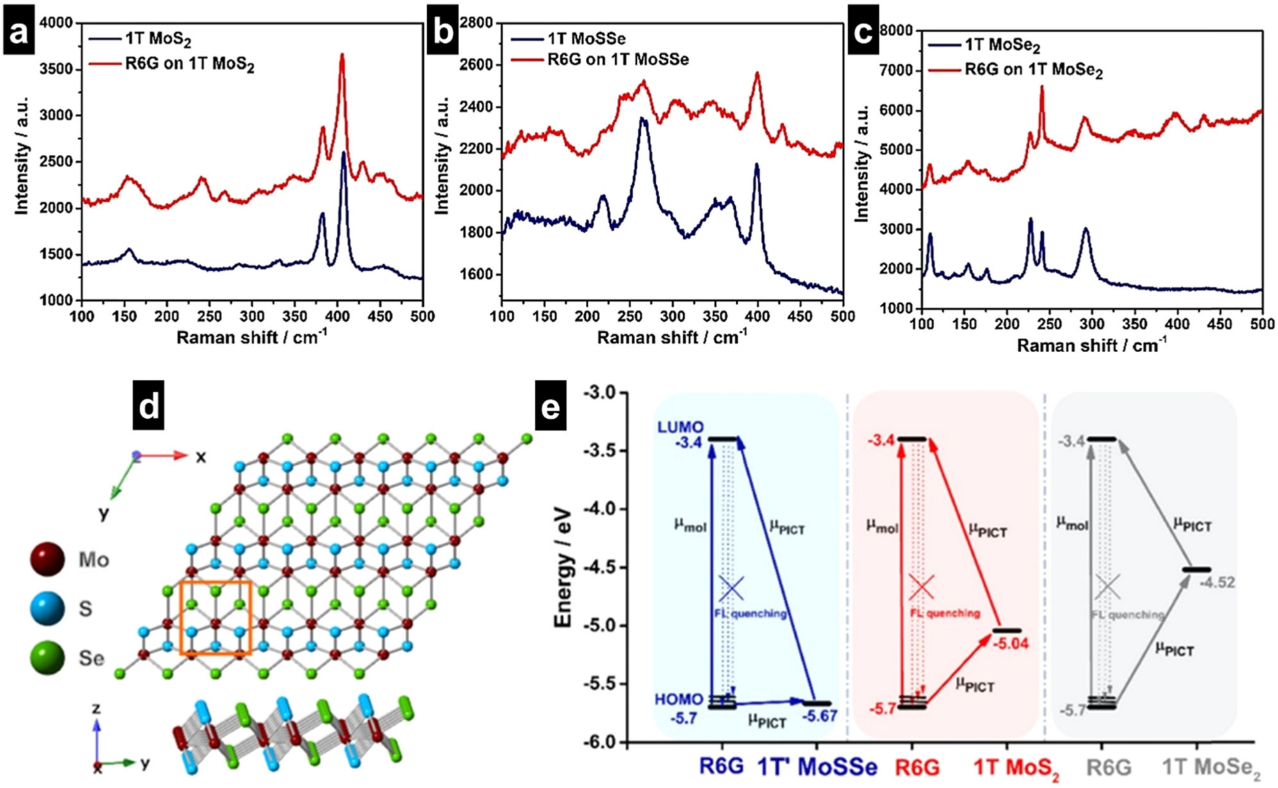

Fig. 4 SERS spectra of the analyte R6G molecules on MoS$_2$ (a), MoSSe (b), and MoSe$_2$ (c) platforms. The top and side views of the optimized 1T MoSSe structure (d) and the possible charge-transfer transition processes in R6G-MoSSe/MoS$_2$/MoSe$_2$.[57] Reprinted with permission from ref. 57 Copyright 2023, American Chemical Society.

Raman signal intensity of up to ~10^6 from model dye molecules (*i.e.*, R6G, methylene blue-MB, crystal violet-CV, and acid blue-AB) on a platform and in a solution medium.[59] Based on their observations, the signal enhancement in Raman spectroscopy occurs at localized areas of intense electromagnetic fields on the MXene surface. These localized spots are believed to arise from the excitation of electrons within the MXene platform to empty energy levels associated with the functional groups attached to its surface. Subsequently, these excited electrons can transfer to the analyte molecules adsorbed on the MXene, further amplifying their Raman signals. Besides MXenes, metal–organic frameworks, or MOFs for short, are a recently developed class of exciting materials.[102–104] MOFs are very promising materials for SERS applications due to their huge potential resulting from structural versatility. Therefore, it is possible to modify the design of a MOF (*i.e.* metal center/organic bridge and topology) to optimize the charge transfer interactions between the analyte and the SERS substrate, which ultimately drives the SERS signal enhancement. In addition, the porous structure of MOFs enhances the adsorption of analytes onto the SERS substrate due to the intrinsic high surface area, which allows us to reach lower detection limits. For example, Sun *et al.* evaluated the Raman signal enhancement performance of three cobalt-based MOFs with different organic linkers, including ZIF-67, Co-TCPP, and Co-MOF-74, TCCP-based MOFs with different metal ions such as Co-TCPP, Cu-TCPP, and Zn-TCPP, and ZIF-8 using R6G as a model target molecule.[60] By manipulating the metal centers and organic ligands, they demonstrated that the combination of the molecular resonance of R6G, the interband transition resonance of MOFs, and the charge-transfer resonance are mainly responsible for the prominent SERS enhancement. This work sheds light on MOF-based target-specific SERS platforms without plasmonic nanoparticles. In 2013, Lee *et al.* also used MIL-100 and MIL 101, having Al^{3+}/Cr^{3+} metal ions and 1,3,5-benzenetricarboxylate/1,4-benzenedicarboxylate organic linkers, as SERS platforms.[105] These MOFs exhibited SERS activity against methyl orange (MO) analyte molecules without any plasmonic metal nanoparticles. SERS signals of MO were still observable even after removing organic linkers with O_2 plasma and high-temperature treatments. This revealed that the SERS active sites in a MOF are the metal oxide clusters and not organic ligands, meaning that charge transfer occurs between the metal cluster part in MIL-100/MIL 101 and the MO analyte molecule. UV-vis spectroscopy measurements of MOFs (MIL-100 and MIL 101), the analyte (MO), and MO–MOF complexes exhibited a profile that is far away from the laser excitation wavelength (632.8 nm). This eliminated the possibility of the resonance enhancement as the main factor of the SERS signal enhancement and made charge transfer-based CM the only plausible way. To further understand the charge-transfer process and orientation dependency of the analyte, the authors used TD-DFT calculations. Consistent with the experimental results, the orientation of the analyte during the adsorption process was found to affect the SERS results due to the change in possible intermolecular interactions. The majority of MOFs used in SERS served as a skeleton for plasmonic metal nanoparticles due to their porous 3D structure, where plasmonic metal particles made the biggest contribution to the enhancement of the SERS signal. To this end, Li *et al.* in 2020 reported an MIL-100 (Fe) based SERS platform, which was developed as a promising volatile organic compound (VOC) detector.[106] MIL-100 (Fe) exhibited an EF of 10^5 with a charge-transfer based CM mechanism and an LOD of ≈ 2.5 ppm against the toluene analyte, which was further improved to a LOD of 0.48 ppb and an EF of 10^{10} in the presence of Au nanoparticles. The authors also used a MIL-100 (Fe) based SERS platform to monitor gaseous biomarkers in the early diagnosis of lung cancer. This SERS active platform holds huge potential to improve detection performance against various VOCs due to its possible modification with other metals, which can form active adsorption sites that enhance the SERS signal intensity.

3. Organic-based SERS platforms

Organic compounds have played a significant role in materials science and nanotechnology over the past several decades, thanks to the carbon's unprecedented ability to form stable bonds with carbon/hydrogen and numerous heteroatoms in diverse electronic forms. This has resulted in significant structural and property versatility, allowing countless organic compounds to be used in various fields, from pharmaceutical chemistry to optoelectronics. Considering all the possible structural and electronic characteristics of organic materials, small molecules and polymers composed of sp^2 hybridized carbon atoms and delocalized π-bonds are indeed excellent candidates for observing the Raman signal enhancement effect.[107] The presence of mobile π-electrons that delocalize over a large group of atoms enables an effective interaction with electrical fields or photons, which can facilitate intra- or intermolecular charge transfer processes. Furthermore, relatively high-lying (un)occupied π-orbitals can be involved in the formation of new charge-transfer states with other organic molecules. The development of next-generation optoelectronics, sensors, and biochemical applications has been influenced by both of these above-mentioned processes. Similarly, the formation of new charge-transfer states and/or intermolecular charge-transfer between two dissimilar organic compounds---one being the SERS platform molecule and the other being the analyte—can open effective pathways for chemical enhancement mechanisms. Despite the attractive characteristics of π-systems for the chemical enhancement mechanism in Raman spectroscopy, organic compounds have not been involved in the design of SERS-active platforms for several decades following the discovery of the SERS effect in the 1970s.

When considered for SERS applications, π-conjugated organic systems offer several key advantages compared to metallic or inorganic-based materials: (i) their molecular energy levels and corresponding light–matter interactions can be fine tuned through small structural modifications on the organic skeletons, providing great versatility for optical properties and SERS sensing, (ii) organic structures can be tailored to achieve molecular-specific interactions in SERS, a direction largely unexplored with metallic and inorganic platforms, (iii) organics can be biocompatible and be easily processed from their solutions in organic solvents into nanostructures, including the use of environmentally friendly solvents,[108] (iv) the scale-up synthesis and straightforward purification of organics could potentially yield low-cost SERS materials, (v) as organic compounds are held together in the solid state *via* relatively weak intermolecular interactions such as dispersion forces, dipolar interactions, and various π-interactions (*e.g.*, "CH···π", "π···π", and "heteroatom···π" contacts), convenient physical processing methods (*e.g.*, physical vapor deposition under vacuum and dissolution) can disrupt these intermolecular forces and lead to unique nano-arrangements on low-cost substrates such as plastic and paper. Here, we also note that, despite early estimations for enhancement factors in the range between 10 and 1000 for metallic structure-based chemical enhancement mechanisms, organic SERS platforms have currently demonstrated enhancement factors of $>10^5$. This is another unique property of organic-based SERS platforms that their highly delocalized π-orbital wave functions enable efficient intermolecular overlaps to facilitate a strong short-range CE effect (*i.e.*, amplification of the analyte polarizability derivative tensor). The very first examples of Raman enhancement on an organic surface were demonstrated in the 2010s using mono- and few-layer graphene substrates, either in their pure form[88] or p-doped with oxygen-containing functional groups.[109,110] These early SERS studies with graphene have inspired our research group to explore organic molecular semiconductors for fabricating SERS-active micro-/nano-structured films. Initially, we used micro-/nano-structured molecular semiconductor films as low-energy (*i.e.*, relatively hydrophobic compared to inorganic oxides) and high surface area templates for depositing metallic structures for the EM enhancement.[111,112] Later, between 2017 and 2021, we successfully demonstrated that undoped molecular semiconductor films could achieve enhancement factors of $>10^5$ in SERS.[113–115] Our pioneering studies have recently been followed by new findings from different research groups and several other small molecule-based SERS platforms with different structures and properties have been demonstrated. On the other hand, polymeric SERS platforms have recently emerged as a new direction. These surfaces do not rely on crystallinity for π-extension through intermolecular packing; rather, polymers have intrinsically extended π-backbones.[116,117] Finally, other specialized organics, including graphene quantum dots, quantum organic semiconductors, and covalent organic frameworks, have been explored in SERS studies. Herein, we provide an overview of the design and development of organics-based SERS platforms and their use in sensing applications, all conducted over the past 15 years (Fig. 5 and Table 2). These

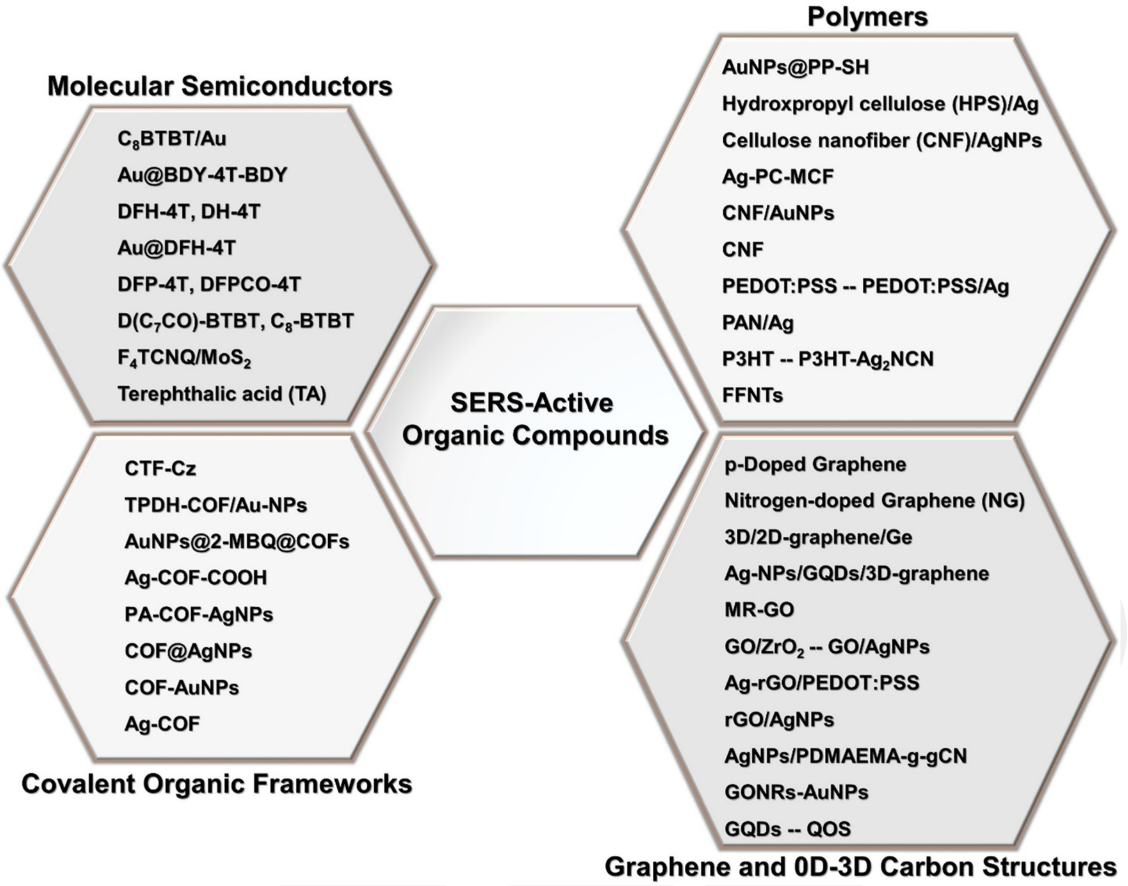

Fig. 5 Summary of the SERS-active organic compounds divided into molecular semiconductors (C_8BTBT/Au,[112] Au@BDY-4T-BDY,[111] DFH-4T/DH-4T,[113] Au@DFH-4T,[113,118] DFP-4T/DFPCO-4T,[114] D(C_7CO)-BTBT/C_8-BTBT,[115] F_4TCNQ/MoS_2,[76] and terephthalic acid[119]), polymers (AuNPs@PP-SH,[120] hydroxypropyl cellulose (HPS)/Ag,[121] cellulose nanofiber (CNF)/AgNPs,[122] Ag-PC-MCF,[123] CNF/AuNPs,[124] CNF,[125] PEDOT:PSS,[126,127] PEDOT:PSS/Ag,[128] PAN/Ag,[129] P3HT,[130] P3HT-Ag_2NCN,[131] and FFNTs[132]), covalent organic frameworks (CTF-Cz,[133] TPDH-COF/Au-NPs,[134] AuNPs@2-MBQ@COFs,[135] Ag-COF-COOH,[136] PA-COF-AgNPs,[137] COF@AgNPs,[138]COF-AuNPs,[139] Ag-COF,[140] and AuNPs/COFs[141]), and graphene/0D-3D carbon nanostructures (graphene,[88] p-doped graphene,[109] nitrogen-doped graphene (NG),[90] 3D/2D-graphene/Ge,[91] Ag-NPs/GQDs/3D-graphene,[142] MR-GO,[110] GO/ZrO_2,[75] GO/AgNPs,[143] Ag-rGO/PEDOT:PSS,[144] rGO/AgNPs,[145] rGO/AgNDs,[146] AgNPs/PDMAEMA-*g*-gCN,[147] GONRs-AuNPs,[148] GQDs,[149] QOS,[150] and rGO/Ag-NPs[151]) that are discussed in this Review.

SERS studies are presented and discussed in four main families based on the structural classifications of the SERS-active organic compounds: (i) molecular semiconductors, (ii) polymers, (iii) covalent organic frameworks, and (iv) graphene and 0D–3D carbon structures (Fig. 5).

3.1. Molecular semiconductor-based SERS platforms

Among the various classes of SERS-active organic compounds, molecular semiconductors offer significant advantages, including reproducible synthesis with convenient purification, minimal batch-to-batch variation, high chemical purity, excellent crystallinity, and versatile processing through solution or vapor-phase methods into micro-/nano-structures. Additionally, small functionalizations or substitutions on the molecular π-core allow for precise tuning of the chemical, electronic, and optical properties, enabling molecule-specific Raman enhancement. The first examples of molecular semiconductor-integrated SERS platforms were demonstrated between 2015 and 2017 in two different studies by Demirel, Usta, and Facchetti *et al.* In both studies, micron-thick, crystalline molecular semiconductor films were used as low-energy, high-surface-area substrates for the deposition of plasmonic thin Au layers. These molecular semiconductor films were prepared in their 3D micro-/nano-structured morphologies using a straightforward physical vapor deposition (PVD) method. In the first study,[112] a fused thienoacene molecule, C_8-BTBT, was employed due to its good thermal and chemical stability, volatility, and facile crystallization behavior into film microstructures. During the fabrication of C_8-BTBT films *via* PVD, it was found that the film morphology largely depends on the deposition angle. A densely packed, ribbon-like 3D microstructure with vertical alignments (*i.e.*, island growth mechanism) was achieved at a deposition angle of 90°. The unique vertical crystal growth was facilitated by the tilted molecular arrangement ($\sim 40^\circ$ tilting from the substrate normal) of C_8-BTBT molecules on the substrate surface, forming π-interactions in the out-of-plane direction. This arrangement was quite different from the C_8-BTBT thin films fabricated for OFETs in earlier

Table 2 Organic-based SERS platforms

Substrate	Analyte molecule	Detection limit/working concentration (M)	Enhancement factor (EF)	Deposition method	Ref.
Molecular semiconductors					
C_8BTBT/Au	MB	10^{-3}	2.1×10^8	Physical vapor deposition (PVD)	112
Au@BDY-4T-BDY	MB	10^{-3}	1.7×10^6	Electrospraying	111
DFH-4TAu@DFH-4T	MB and R6G MB	10^{-5} $<10^{-21}$	3.4×10^3 and 2.1×10^2 $\sim 10^{10}$	PVD	113
Au@DFH-4T	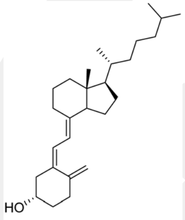 Cholecalciferol	10^{-10}	—	Thermal evaporation (TE)	118
DFP-4T	MB	10^{-9}	$>10^5$	PVD	114
D(C_7CO)-BTBT	MB, R6G, CV, and 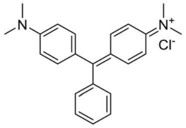 Malachite Green (**MG**)	10^{-3}	$>5 \times 10^3$	PVD	115
F_4TCNQ/MoS_2	MB	10^{-10}	2.53×10^6	PVD	76
Terephthalic acid (TA)	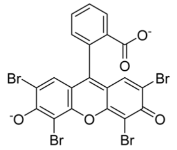 Eosin Y (**EY**)	0.5×10^{-6}, 10^{-6}, and 10^{-6}	1.50×10^6, 3.23×10^4, and 7.17×10^4	Drop-casting	119
Polymers					
AuNPs@PP-SH	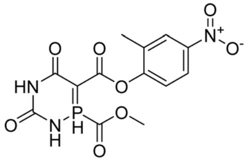 *p*-cresol	—	—	Spin-coating	120
Hydroxpropyl cellulose (HPS)/Ag	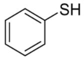 thiophenol	—	—	Soft lithography/TE	121
Cellulose nanofiber (CNF)/AgNPs	R6G	$<10^{-6}$	3×10^6	Silver mirror reaction	122
Ag-PC-MCF		$<10^{-6}$	—	Etching	123

Table 2 (*continued*)

Substrate	Analyte molecule	Detection limit/working concentration (M)	Enhancement factor (EF)	Deposition method	Ref.
Molecular semiconductors					
CNF/AuNPs	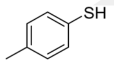 p-methylthiophenol 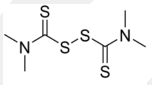 thiram	5.2×10^{-10}	—	—	124
CNF	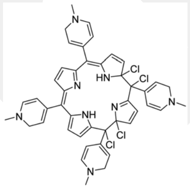 meso-tetra(N-methyl-4-pyridyl)porphine tetrachloride (TMPyP)	$\sim 10^{-5}$	10^{2}	Drop-casting	125
PEDOT:PSS	MB	—	2.26×10^{3}	Spin-coating	127
PEDOT:PSS	MB	10^{-3}	4.0×10^{2}–1.0×10^{3}	Spin-coating	126
PEDOT:PSS/Ag	4-MBA	10^{-3}	–	Drop-casting	128
PAN/Ag	4-MBA	10^{-3}	—	Spin-coating	129
P3HT	MB	10^{-6}	94–848	Spin-coating	130
P3HT-Ag_2NCN	MB	10^{-8}	6147	Spin-coating	131
FFNTs	MB	10^{-7}	7	Drop-casting	132
Covalent organic frameworks					
CTF-Cz	R6G	10^{-6}	$\sim 10^{5}$ (9.1×10^{4})	—	133
TPDH-COF/Au-NPs	R6G	10^{-10}	2.01×10^{8}	Drop-casting	134
AuNPs@2-MBQ@COFs	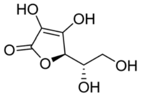 Ascorbic Acid (**AA**) and ClO^{-}	0.66×10^{-6}	—	—	135
Ag-COF-COOH	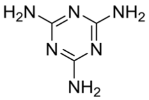 Melamine	10^{-9}	2.49×10^{8}	—	136
PA-COF-AgNPs	Hg^{2+}	2×10^{-11}	—	—	137
COF@AgNPs	MG	1.04×10^{-10}	1.4×10^{6}	—	138
COF-AuNPs	MG and Thiram	6.2×10^{-10} and 1.7×10^{-8}	1.13×10^{6}	Drop-casting	139

Table 2 (*continued*)

Substrate	Analyte molecule	Detection limit/working concentration (M)	Enhancement factor (EF)	Deposition method	Ref.
Molecular semiconductors					
Ag-COF	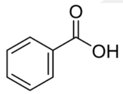 Benzoic Acid	1.06×10^{-6}	—	—	140
AuNPs/COFs	SARS-CoV-2 S protein	2.7×10^{-16} (g mL^{-1})	—	—	141
Graphene and 0D–3D carbon structures					
Graphene	Pc, R6G, PPP, and CV	10^{-8}–10^{-10}	2–17	Vacuum evaporation and solution-soaking	88
p-Doped graphene	RhB, R6G and CV	10^{-5}	$\sim 10^{4}$	CVD and Uv-Ozone	109
Nitrogen-doped graphene (NG)	RhB, CV, and MB	10^{-11}	$\sim$2–16	AP-CVD	90
3D/2D-graphene/Ge	RhB, R6G, MB, Mel, and 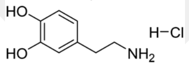 3-hydroxytyramine hydrochloride (3-HH)	10^{-8}–10^{-10}	—	CVD/PACVD	91
Ag-NPs/GQDs/3D-graphene	R6G, MB, TMTD, MP, and 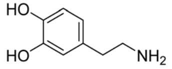	10^{-7}–10^{-11}	—	PACVD	142
MR-GO	RhB	—	$\sim 10^{3}$	Drop-casting	110
GO/ZrO_2	Methyl parathion	0.12×10^{-6}	8.78×10^{4}	Drop-casting	75
GO/AgNPs	RhB	10^{-10}	3×10^{10}—5×10^{10}	Dip-coating	143
Ag-rGO/PEDOT:PSS	MB	10^{-8}	—	Spin-coating	144
rGO/AgNPs	MB	10^{-8}	4.6×10^{5}	Immersing	145
rGO/AgNDs	MB	10^{-7}	2299	Galvanic replacement and spin-coating	146
AgNPs/PDMAEMA-*g*-gCN	R6G	10^{-8}	2.4×10^{7}	Thermal oxidative etching and SIPGP	147
GONRs–AuNPs	CV	—	—	Drop-casting	148
GQDs	R6G	$<10^{-9}$	$>10^{3}$	PECVD	149
QOS	R6G and CV	10^{-15}	10^{12}	fs Laser pulse irradiation with low-pressured N_2 gas	150
rGO/Ag-NPs	MB	10^{-9}	$\sim 10^{8}$	Immersing	151

studies.[152] This low-energy, high-surface-area substrate was used as the template platform for the deposition of a nanoscopic thin Au layer (~32 nm) *via* thermal evaporation under vacuum. The C_8-BTBT/Au bilayer platforms demonstrated excellent SERS activity with the methylene blue analyte, achieving a high Raman signal enhancement factor of 2.1×10^8. Additionally, these substrates showed good stability (>90 days) and reproducibility (relative standard deviation < 0.14). In their second study, Usta and Demirel *et al.* explored a solution-based fabrication strategy for fabricating SERS-active substrates.[111] The main motivation behind this study was to integrate a facile electrospraying method for the growth of 3D micro-/nanostructured BDY-4T-BDY molecular semiconductor films. An acceptor–donor–acceptor type molecular π-architecture with a 4,4-difluoro-4-bora-3a,4a-diaza-*s*-indacene (BODIPY) terminal acceptor and quaterthiophene donor units was employed. Highly uniform dendritic nanoribbons with vertically oriented nanoplates and sharp needle-like tips were deposited on flexible, regular aluminum foil (5 cm × 5 cm) by electrospraying molecular semiconductor solutions in a $CHCl_3$/dimethylformamide (DMF) (2 : 1) mixture. This organic template was later coated with a nanoscopic thin Au layer (~30 nm). The interaction between the organic semiconductor and the analyte was enhanced due to the abundance of adsorption sites, while needle-like tips in the films created hot spots, ultimately increasing the Raman signal. Enhancement factors of up to 1.7×10^6 for the MB analyte molecule were achieved. Both studies have revealed the great potential of molecular semiconductor-metallic thin-film bilayer platforms in SERS applications. These platforms could enable low-cost and convenient fabrication of SERS-active substrates on various materials, including plastics and paper. Following these studies, a main question still remained: could a nanostructured organic semiconductor film enable efficient Raman enhancement without the need for a metallic layer?

The studies conducted by Demirel, Usta, and Facchetti *et al.* between 2017 and 2021 have focused on developing purely molecular semiconductor films for the Raman enhancement. In these studies, six different semiconducting molecules have been explored as SERS substrates. These molecules have been extensively characterized as both n- and p-type semiconductors in various (opto)electronic devices in earlier research.[153] They were chosen for their good volatility for physical vapor deposition, chemical/thermal stability, and efficient charge transfer characteristics. Additionally, a systematic molecular engineering approach was adopted from the initial study in 2017 to subsequent ones in 2019 and 2021. This approach aimed to elucidate the effect of the molecular π-architecture, substitutions, functionalizations, and the electronic structure on the fabrication and SERS activity of the corresponding platforms. In the initial study in 2017,[113] DFH-4T was introduced as the first π-conjugated molecular semiconductor for the efficient Raman enhancement. This molecule is an n-type organic semiconductor with a stabilized LUMO energy level of −3.2 eV, and it is based on a quaterthiophene π-core, having perfluorohexyl side chains at α,ω-positions. The film deposition *via* PVD was performed using an ultra-fast deposition rate (>40 nm s^{-1}) at a short distance (~5–7 cm), promoting out-of-plane crystal growth. This method enabled the creation of an ivy-like nanostructured superhydrophobic semiconductor film (water contact angle ≈ 152°), with molecular π-cores available for charge-transfer interactions with effectively adsorbed analyte molecules. DFH-4T films exhibited an unprecedented Raman signal enhancement of 3.4×10^3 for the probe molecule MB, which is remarkable considering that no additional plasmonic layer was used in this study. Quantum mechanical computations, comparative experimental studies with DH-4T (a fluorocarbon-free α,ω-dihexylquaterthiophene molecule), and film microstructural analysis revealed the critical role of the DFH-4T's molecular structure, frontier molecular orbitals, and 3D highly textured morphology in facilitating a resonance charge transfer mechanism for the observed Raman enhancement. In this study, when the fabricated superhydrophobic DFH-4T substrates were combined with a thin Au layer, a Raman signal enhancement of $\sim 10^{10}$ and a sub-zeptomole ($<10^{-21}$ mole) analyte detection limit were accomplished. This was due to the formation of closely packed plasmonic Au nanoparticles (~9–16 nm), which initiated the electromagnetic enhancement mechanism as the main driving force in the Raman enhancement. This part of the work has opened a new avenue in single-molecule detection with high Raman signal enhancement by fabricating organic semiconductor-metallic bilayer platforms through a simple PVD process. Very recently, Liu *et al.* prepared flexible polydimethylsiloxane (PDMS) membranes embedding Au-DFH-4T hybrid nanostructures for detecting hydrophobic biomolecules at low concentrations.[118] The evaporation of both the organic semiconductor and metallic layers was performed *via* simple thermal evaporation under vacuum onto a nitrogen plasma-treated polydimethylsiloxane (NP-PDMS) membrane. Here, the nitrogen plasma treatment resulted in a relatively hydrophilic PDMS surface with higher roughness compared to untreated PDMS, which enhanced the adhesion to DFH-4T nanostructures. To tune the SERS activity and selectivity, Au layers of different thicknesses (5–20 nm) were deposited, and a 15 nm-thick Au layer was found to exhibit the highest SERS performance due to its optimal film morphology characterized by the absence of aggregation and small grain-based nanostructures, enabling the formation of enormous hot spots effects. The same platform exhibited very sensitive SERS activity against cholecalciferol (Vitamin D_3) with a limit of detection less than 10^{-10} M. On the other hand, this flexible SERS platform was shown to be mechanically stable, as it maintains its SERS performance after 100 cycles of bending. These findings in this study have the potential to expand the applications of SERS platforms to flexible, wearable technologies, especially enabling the detection of biomolecules.

In their second study, building upon the highly promising results achieved with DFH-4T, Demirel, Usta, and Facchetti *et al.* have focused on engineering the π-architecture of the quaterthiophene system.[114] The new SERS molecule, DFP-4T, comprises a fully π-conjugated diperfluorophenyl-substituted

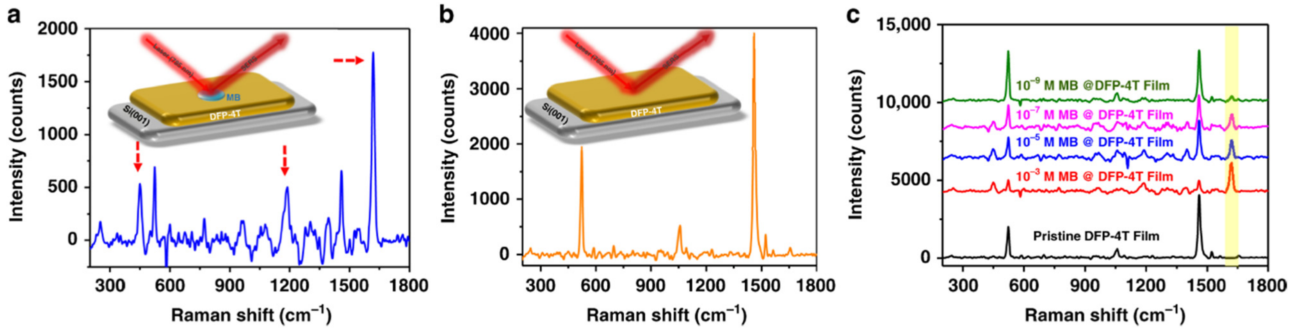

Fig. 6 The SERS spectra of the methylene blue analyte molecule on the nanostructured DFP-4T-based molecular semiconductor substrate showing the characteristic Raman peaks (10^{-3} M in "a" and different analyte concentrations (10^{-3}–10^{-9} M in "c") and the SERS spectrum of the pristine nanostructured DFP-4T molecular semiconductor substrate (b).[114] Reprinted with permission from ref. 114 Copyright 2019, Springer Nature.

quaterthiophene structure, facilitating an uninterrupted π-system that extends across the entire molecular structure (interring torsion angles $< 18°$). The primary modification in this study, compared to the previous one, involved replacing the σ-insulating perfluoroalkyl chains with perfluorophenyl π-units, which was found to enhance π-overlaps and charge-transfer interactions between the substrate and the analyte molecules. The nanostructured DFP-4T films, grown *via* the PVD process, exhibited a significant Raman enhancement factor (EF) of $> 10^5$ and a low limit of detection (LOD) down to 10^{-9} M for the MB analyte molecule (Fig. 6). This EF is comparable to those reported for the best inorganic semiconductor SERS platforms. The notable SERS enhancement is attributed to a resonance charge-transfer mechanism between the face-on oriented DFP-4T molecules in the nanostructured film and the MB probe molecule. This was corroborated by spectroscopy experiments and electronic structure calculations. In the same study, a carbonyl-functionalized comparative molecule, DFPCO-4T, was also employed as the SERS platform. DFPCO-4T yielded a higher density of face-on oriented domains, and the incorporation of electron-withdrawing carbonyl functionalities not only lowers the molecular HOMO/LUMO energetics but also limits the wave function delocalizations only on the central quaterthiophene π-backbone. Thus, analyte molecules interacting with the end groups of DFPCO-4T or DFH-4T will be unable to couple with the SERS substrate for charge transfer processes effectively. Additionally, the CT resonance energy deviates from the laser excitation wavelength for both of these molecules, limiting EFs to $\sim 10^3$ for both systems. The highly delocalized frontier orbital wave functions of DFP-4T enable appropriate orbital overlaps with analyte π-systems and appropriate charge-transfer energies aligning with the laser excitation energy. This leads to a small but non-zero oscillator strength in the charge-transfer state, which is effective enough to enhance the polarizability derivative tensor of analyte vibrational modes.

In 2021, Usta, Demirel, and colleagues used a different strategy to reveal the underlying molecular orbital interactions in the chemical enhancement mechanism of organic semiconductors in SERS.[115] In this study, they employed a fused thienoacene π-core functionalized with carbonyls along the long molecular axis. This molecular semiconductor, D(C_7CO)-BTBT, showed an extended π-conjugation involving in-plane oriented carbonyl units, yielding a highly stabilized LUMO (−3.54 eV) compared to that of the well-known C_8-BTBT (−2.10 eV). The vapor-deposited D(C_7CO)-BTBT film microstructure and morphology revealed that the polar functional groups facilitate the out-of-plane crystal growth *via* a zigzag motif of dipolar $C{=}O\cdots C{=}O$ interactions and hydrogen bonds. Additionally, π-interactions between thienoacene π-cores were found to be strengthened after carbonyl functionalization due to enhanced electron deficiency. The D(C_7CO)-BTBT's film growth behavior was identified to occur in two stages, starting with an edge-on oriented molecular arrangement (*i.e.*, face-on domain growth) on the high energy substrate surface and transitioning to a face-on molecular orientation (*i.e.*, edge-on domain growth) after reaching a certain surface hydrophobicity (Fig. 7).

Significant Raman enhancements were observed on the D(C_7CO)-BTBT's highly porous 3D crystalline surface with four different analyte molecules (methylene blue (MB), rhodamine 6G (R6G), crystal violet (CV), and malachite green (MG)), showing Raman intensities of up to ∼4000–5000 (Fig. 8). The study of electronic structures and anti-Stokes/Stokes SERS signal ratios indicates that the chemically enhanced mechanism is primarily influenced by the π-extended and stabilized LUMO of D(C_7CO)-BTBT and the varied crystalline face-on orientations in the semiconductor film. When the carbonyl units are removed in C_8-BTBT, the semiconductor's relatively high-lying LUMO prevents effective frontier orbital mixing with the analyte molecules, and also only a 2D domain growth was observed on the substrate surface. Consequently, the Raman enhancement on C_8-BTBT was much weaker, and it was only observed with MB, as it has the lowest LUMO among other analytes, allowing for an energetically feasible resonant transition (photoinduced charge transfer at 1.50 eV for $\mathrm{HOMO}_{\mathrm{C8\text{-}BTBT}} \rightarrow \mathrm{LUMO}_{\mathrm{MB}}$). This suggests that the molecular specificity in organic semiconductor-based SERS platforms could be tuned through the frontier orbital energetics of the corresponding semiconductor and analyte molecules.

Following the excellent results achieved with oligothiophenes and thienoacene π-systems in SERS activity, Liu and

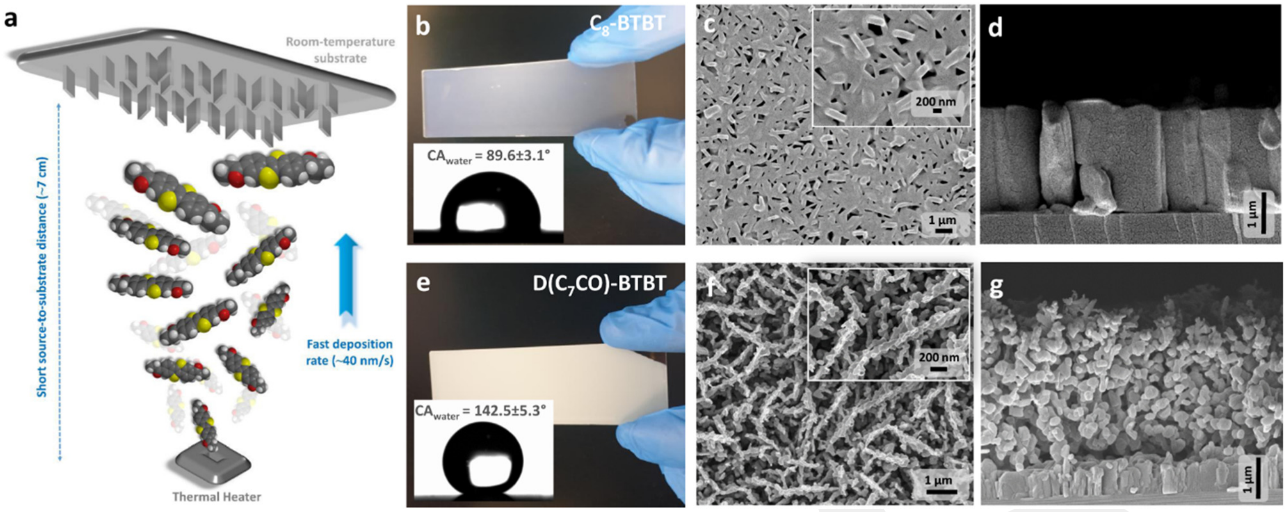

Fig. 7 (a) Schematic diagram depicting the physical vapor deposition (PVD) technique and the critical parameters involved in fabricating nanostructured SERS films. Images (b) and (e) show the nanostructured films and a water droplet on their surface, including water contact angles (CA_{water}). Top-view and cross-sectional SEM images of C_8-BTBT (c) and (d) and D(C_7CO)-BTBT (f) and (g) nanostructured films are also provided.[115] Reprinted with permission from ref. 115 Copyright 2021, Springer Nature.

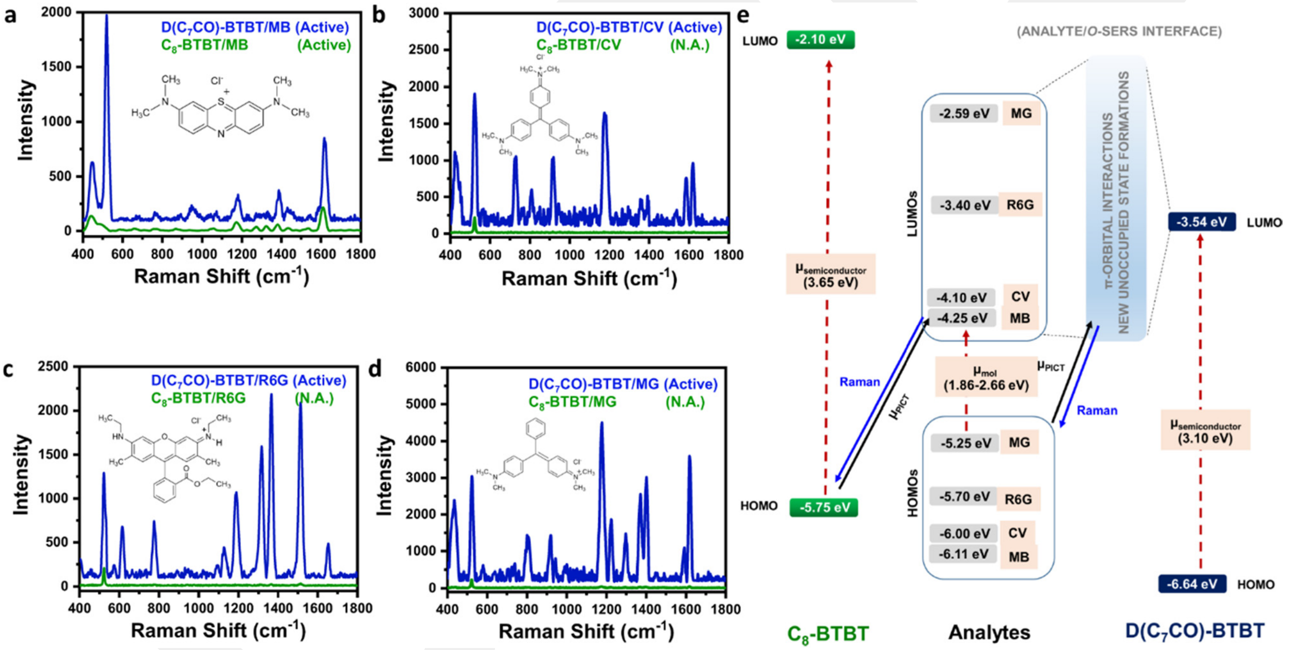

Fig. 8 The SERS spectra of methylene blue (MB) (a), crystal violet (CV) (b), rhodamine 6G (R6G) (c), and malachite green (MG) (d) on D(C_7CO)-BTBT and C_8-BTBT films. The insets illustrate the molecular structures of the analytes. Panel (e) presents the energy level diagram (in a vacuum) for the analyte/semiconductor systems, detailing the frontier molecular orbitals (HOMO/LUMO) and indicating likely (solid black arrows) and unlikely (dashed red arrows) electronic transitions. μ_{PICT} represents photoinduced charge transfer between the analyte and the semiconductor molecules when excited at 785 nm. Raman signals resulting from the transitions are indicated by solid blue arrows.[115] Reprinted with permission from ref. 115 Copyright 2021, Springer Nature.

Zhang *et al.* explored a new approach in 2022. They modified a two-dimensional MoS_2 flake surface with two different molecular organic semiconductors, 2,5-difluoro-7,7,8,8-tetracyanoquinodimethane (F_2TCNQ) and 2,3,5,6-tetrafluoro-7,7,8,8-tetracyanoquinodimethane (F_4TCNQ), and used these platforms for SERS.[76] These molecules were chosen for their strong electron-accepting nature, while the underlying 2D MoS_2 structure was employed for its charge-localization effect. While the MoS_2 flakes with an ultra-flat surface were grown *via* chemical vapor deposition, F_nTCNQ nanoparticles (∼20–25 nm in lateral size) were deposited onto these flakes *via* physical vapor deposition (Fig. 9). In this study, by comparing

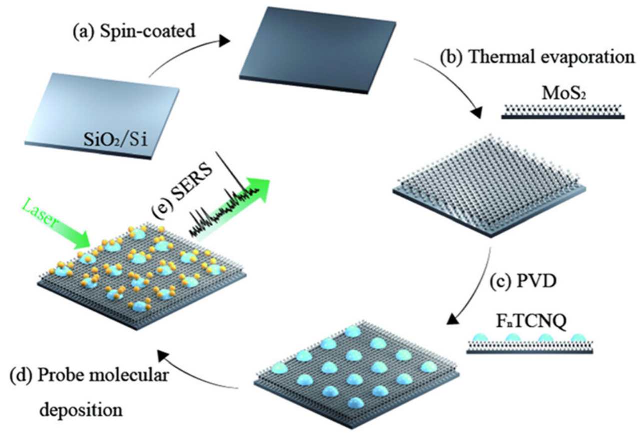

Fig. 9 Diagram of the fabrication steps (a)–(c) and the SERS process (d) and (e) of the hybrid F_nTCNQ/MoS_2 nanocomposites.[76] Reprinted with permission from ref. 76 Copyright 2022, American Chemical Society.

F_4TCNQ with F_2TCNQ as the SERS-active molecule, it was found that the number of fluorine atoms governed the charge transfer directions and charge localizations in the composite heterostructure system, which ultimately affected the SERS sensitivities. A strong Raman enhancement of 2.53×10^6 was achieved for the optimal F_4TCNQ/MoS_2 nanocomposite substrate, as well as a low limit of detection value of 10^{-10} M for the non-resonant methylene blue analyte molecule. Along with MB, a resonant molecule, R6G, and an environmental pollutant, 4-aminothiophenol (4-ATP), were detected on the same SERS platform from a mixed solution, showing the versatility of these platforms. The presence of the F_nTCNQ/MoS_2 composite heterostructure induces the overlapping of molecular orbitals between MoS_2 and C–F bonds, resulting in a charge redistribution and increasing the probability of charge transfer between the analyte and the SERS-active semiconductor molecules. This study provided unique insight into the chemical enhancement mechanism and improved the SERS performance of molecular organic semiconductors by employing a charge-localization effect of a two-dimensional material. The intrinsic SERS activity of other molecular semiconductors could be improved following a similar approach.

Chattopadhyay *et al.* very recently developed a π-conjugated electron-rich terephthalic acid (TA)-based metal-free SERS platform by using molecular microcrystals. This substrate showed Raman enhancement factors of 1.50×10^6, 3.23×10^4, and 7.17×10^4 with limit of detection values of 0.5, 1, and 1 μM for rhodamine-6G (R6G), rhodamine B (RhB), and eosin yellowish (EY) analyte molecules, respectively.[119] In addition, the simultaneous deposition of two different molecules on the substrate caused analyte-specific fluctuation in the SERS signal. It was found that the binary SERS performance observed in this study was heavily related to the electronic structure of the crystal, charge transfer transition upon excitation with a Raman laser, and formation of hybrid orbitals between the analyte and the substrate through non-covalent interactions (*i.e.*, π–π interactions, hydrogen bonding, van der Waals interactions, and halogen bonding). This study demonstrated the great potential of using molecular crystals for the future structural design of SERS-active platforms and molecular specificity. As a final takeaway from this section, it is noteworthy that molecular semiconductors with spatially limited and tunable π-conjugated skeletons provide an excellent ground for extensive structural modifications. These chemical structures can be precisely engineered to optimize charge transfer to specific analyte molecules in SERS applications.

3.2. Polymer-based SERS platforms

Polymers are characterized by their extended π-systems and significantly larger molecular weights compared to small molecules. Additionally, by simply changing the molecular structures or donor–acceptor strengths of the monomers, the physicochemical and electronic properties of polymers can be tuned to meet specific criteria in any application. When considered for SERS applications, their extended backbones provide a large π-interaction surface with analyte molecules without requiring high crystallinity in nano- or micro-structured forms. In addition, the charge carrier separation and delocalization along the polymer π-backbone can be very efficient for the chemical enhancement mechanism in SERS, as it has been widely demonstrated in photovoltaics. Although the synthesis, purification, and batch-to-batch reproducibility of polymers can sometimes be inferior to those of small molecules, processing polymers into films is technically more suitable due to the better rheological properties of polymer solutions. Excitingly, polymers used in SERS applications can be sourced from low-cost, environmentally friendly, and biodegradable natural materials such as cellulose. The use of polymers in SERS applications is relatively new compared to molecular semiconductors, with all relevant studies conducted in the past few years.

The early examples of using polymers in SERS, which are very similar to those studied with molecular semiconductors, involved using polymeric films as templates for the deposition of metallic structures. Therefore, in these early studies, the electromagnetic enhancement was still the main mechanism with polymer-based SERS platforms. In 2019, Chen *et al.* developed a hybrid polymer-based SERS platform having thiol-functionalized poly(3,4-ethylenedioxythiophene) (PEDOT) and Au nanoparticles (AuNPs) to selectively detect *p*-cresol (PC) among various interferers.[120] In this study, the three-dimensional nanostructured polymer surface, on which a uniform, high density of AuNPs (sizes of ∼14.5 ± 1.4 nm) are immobilized, yielded an efficient Raman enhancement due to both efficient hot-spot formations and the increased number of analyte adsorption sites. On the other hand, strong covalent bonding interactions were present between the AuNPs and the thiol-functionalized PEDOT film to realize a robust SERS-substrate. As the test solution, aqueous fluids with dopamine (DA), ascorbic acid (AA), and uric acid (UA) as additional interferers to PC were used, and the selective detection of PC was achieved. This SERS platform also worked as an organic electrochemical transistor (OECT), as it featured a highly conductive underlying PEDOT:PSS film for electrochemical sensing purposes. The performance of the OECTs for the selective detection of dopamine (DA) was improved by the AuNP-immobilized thiol-functionalized PEDOT film as the top interfacial layer. Similar OECT/SERS hybrid biosensors, based on polymeric substrates and active layers, could find use in the design of next-generation biosensors for point-of-care diagnostics.

During the same period, various research groups utilized different polymers, including cellulose nanofibers, in combination with Au or Ag metallic nanostructures to create plasmonic substrates for the Raman enhancement.[121–123] Some of these structures were used for detecting trace analytes, including pesticides and essential biological species, even at concentrations as low as sub-attomolar levels.[122,124] In one of these studies by Mihi *et al.*,[121] eco-friendly and disposable photonic crystals were developed using hydroxypropyl cellulose. These submicron periodic lattices, created through soft lithography, were coated with a 100 nm layer of silver *via* thermal evaporation, resulting in plasmonic structures with hot spots. These structures exhibited excellent Raman signal enhancements for the thiophenol analyte when excited with 532 nm and 633 nm laser wavelengths. Cellulose, composed of D-glucose units linked by glycosidic bonds, is an abundant, sustainable, and biodegradable organic polymer found in nature.

Following the cellulose-metallic bilayer SERS studies, a SERS-active platform that relies solely on a cellulose structure, without the need for a metallic second layer, was recently reported by Rice *et al.* in 2021.[125] Their main motivation was to address the biocompatibility issues associated with noble metals. In their study, they employed metal-free cellulose nanofibers (CNFs), which are nanostructured cellulose arranged into micron-long, one-dimensional structures with both crystalline and amorphous regions. The CNF SERS platform was fabricated by simply drop-casting a nanofiber solution onto a silicon substrate, and five different porphyrin derivatives (two anionic, two cationic, and one hydrophobic), which play a crucial role in the transport and storage of oxygen in blood, have been detected. Notably, a 10^2-fold increase in signal intensity and a limit of detection of $\sim 10^{-5}$ M were observed with the *meso*-tetra(*N*-methyl-4-pyridyl)porphine tetrachloride (TMPyP) analyte (Fig. 10). In this study, more conventional substrates, including graphene oxide (GO) and silicon, were also used for the detection of porphyrin-based molecules, and their SERS performances were found to be inferior to CNF-based substrates (Fig. 10). The observed enhancement is due to the energetically favorable pathways for chemical enhancement *via* photoinduced charge transfers, as well as the disrupted formation of self-assembled structures on the cellulose nanofibers leading to the formation of disordered 3D porphyrin clusters. This study poses an intriguing question in the field of whether polymers lacking π-conjugation systems would also enhance Raman signals. Here, it is still important to note that cellulose nanofibers (CNFs) have a reported low LUMO energy level of −3.57 eV, which enables pathways for photoinduced charge transfers with analytes (Fig. 10(a)).

In another instance of a metal-free polymeric SERS platform, Yang and Chen *et al.* recently explored a π-conjugated conducting polymer, PEDOT:PSS, as a SERS substrate to monitor the carrier dynamics under varying forward/reverse bias voltages

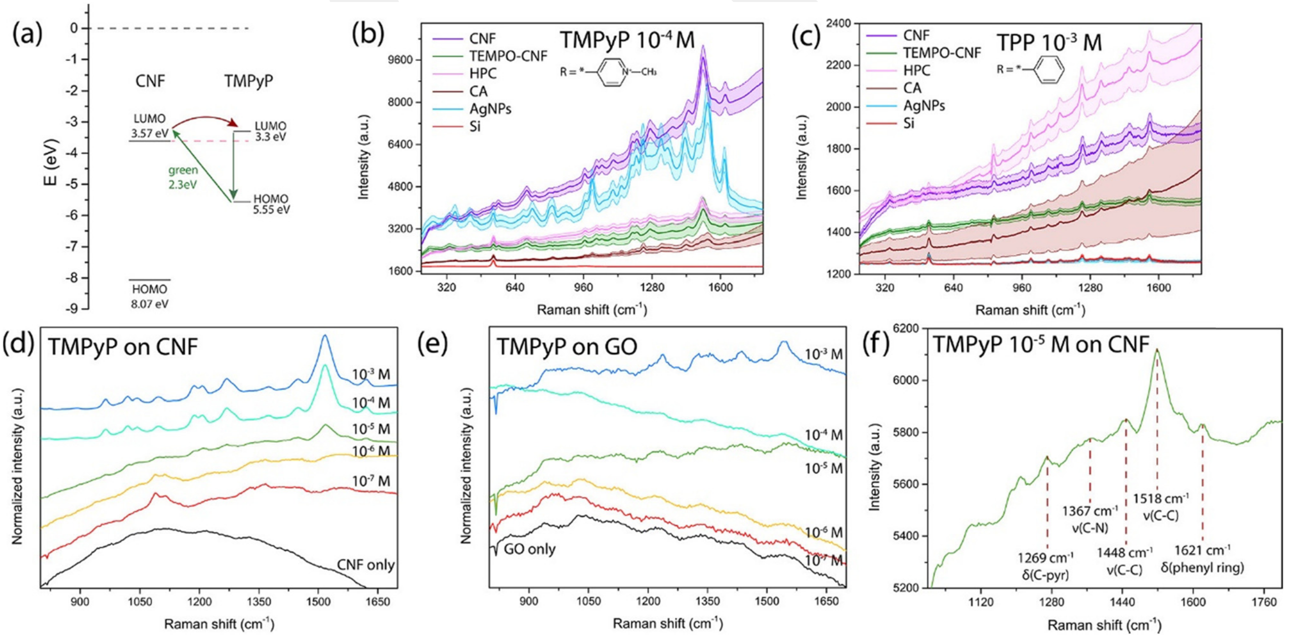

Fig. 10 (a) A proposed energy band diagram illustrating the potential charge transfer process between the CNF substrate and a TMPyP molecule. (b) and (c) SERS spectra of porphyrins on various cellulose-based substrates compared with those on silver nanoparticles and silicon. The normalized SERS spectra of TMPyP on CNF (d) and GO (e). (f) The spectrum of 10^{-5} M TMPyP on CNF, emphasizing the low detection limit achievable with the metal-free polymer substrate.[125] Reprinted with permission from ref. 125 Copyright 2021, American Chemical Society.

and conductivity conditions.[127] The smooth PEDOT:PSS film with an RMS roughness of 1.81 nm ($2 \times 2\ \mu m^2$) showed an EF of 2.26×10^3 for the methylene blue (MB) analyte molecule. Despite its smooth surface, the significant Raman enhancement was attributed to a combination of chemical effects (*via* charge transfer interactions) and electromagnetic effects (arising from surface plasmons due to the polymer's charge carrier density).[154] The intensity of the MB Raman peak at 1625 cm^{-1} increased at a voltage of 0.5 V and gradually decreased as the voltage increased further. Additionally, some of the MB Raman peaks initially exhibited blue shifts followed by red shifts, indicating an increase and a subsequent decrease in carrier density, respectively. This study introduced a novel concept of voltage-dependent SERS platforms to analyze the spectroscopic performance and rectification-like characteristics at semiconductor heterojunctions. The findings are insightful for the implementation of SERS applications in the field of optoelectronic devices. The use of PEDOT:PSS as a SERS platform was recently demonstrated in another study by Jung and Chen *et al.*[126] In their research, SERS-active polymer films were prepared by spin-coating a PEDOT:PSS solution onto a silicon substrate, followed by thermal annealing at different temperatures (Fig. 11). Notably, thermal annealing induced a benzoid-to-quinoid structural transformation in the PEDOT component of the polymer film. Based on DFT calculations, while the spatial distribution of electronic wave functions is mainly localized on the thiophene units in the benzoid structure, an enhanced π-delocalization was evident in the quinoid structure after thermal annealing. This favorable HOMO topology increased the possibility of polymer–analyte intermolecular charge transfer interactions, which ultimately enhanced the Raman signals. As a result, the PEDOT:PSS films annealed at 150 °C exhibited enhancement factors of 4.0×10^2 ($\lambda_{\text{excitation}}$ = 532 nm) and 1.0×10^3 ($\lambda_{\text{excitation}}$ = 633 nm) for methylene blue. This study was the first to show how the π-electron (de)localization in the frontier orbitals of polymers affects SERS activity.

In a different study employing the PEDOT:PSS polymer, Chen and Jung *et al.* developed a sandwich-structured trilayer SERS platform based on Ag nanoparticles, 4-mercaptobenzoic acid (4-MBA) probe molecules, and PEDOT:PSS, which were prepared by layer-by-layer assembly.[128] They investigated the effects of different concentrations of PEDOT:PSS on the Raman signal intensity of 4-MBA. SERS active layers, both without and with the PEDOT:PSS polymer layer, were used to understand the effect of intermolecular hydrogen bonding in the charge transfer process. The degree of the charged transfer process was found to be enhanced upon doping the metal–analyte bilayer system with PEDOT:PSS, due to hydrogen bond interactions between 4-MBA and PEDOT:PSS. The hydrogen bond formation between 4-MBA analyte molecules and PEDOT:PSS facilitated the charge redistribution in the 4-MBA/Ag complex, leading to Raman enhancements. This study disclosed the potential use of organic semiconductors in metallic-based SERS applications, particularly through hydrogen bonding interactions with the analyte molecules. The following year, the same research group developed a similar sandwich-structured trilayer SERS platform, this time employing the conductive polymer polyaniline (PAN) for Raman enhancements through charge transfer.[129] It was found that as the PAN thickness increased, the frequency and intensity of the characteristic

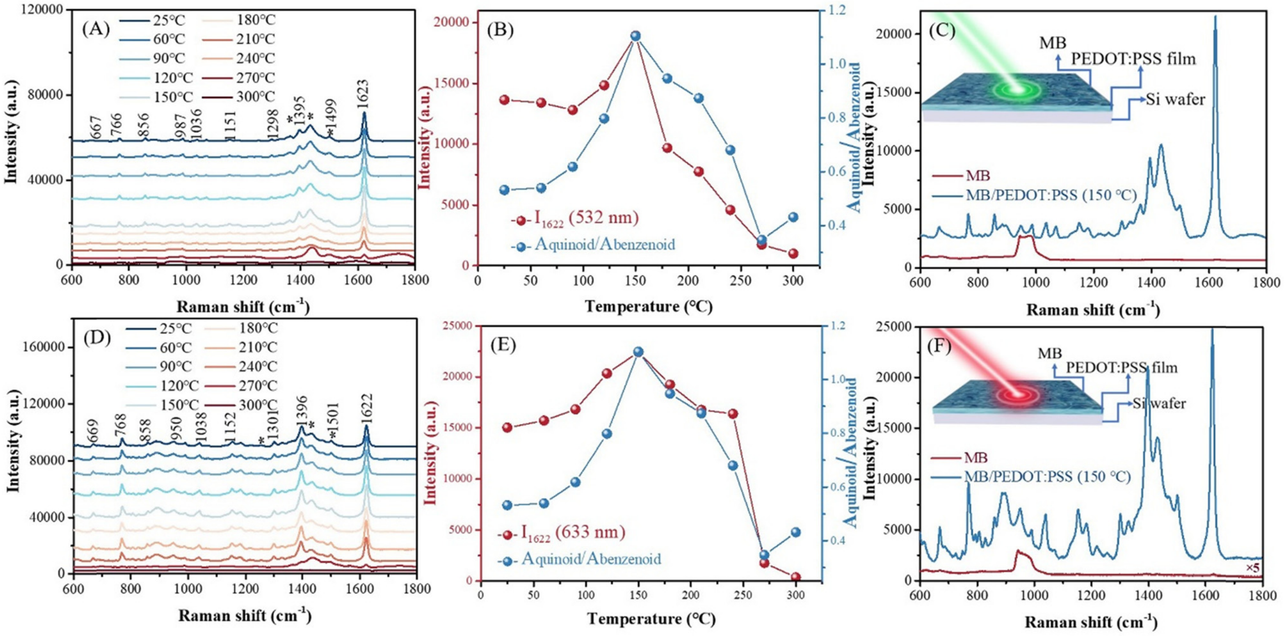

Fig. 11 SERS spectra of MB under 532 nm (A) and 633 nm (D) laser excitations recorded on the PEDOT:PSS film after thermal annealing at different temperatures. (B) and (E) The intensity of the corresponding Raman peaks at 1622 cm^{-1} (red line) is shown along with the PEDOT's resonance structure transition (blue line). The comparative Raman spectra of MB on a Si wafer (red line) and on the PEDOT:PSS film (blue line) under 532 nm (C) and 633 nm (F) laser excitations.[126] Reprinted with permission from ref. 126 Copyright 2023, Wiley-VCH GmbH.

4-MBA bands gradually increased. Based on two-dimensional correlation spectroscopy (2D-COS) measurements, the direction of the charge transfer process was found to occur from the Fermi level of Ag towards the LUMO of 4-MBA and then subsequently to the LUMO of PAN.

In 2022, Chen, Xu, and co-workers developed a SERS-active platform based on a spin-coated regioregular poly(3-hexylthiophene-2,5-diyl) (P3HT) film.[130] Their approach aimed to enhance the crystallinity of the spin-coated P3HT film by immersing it in a binary system of one good and one poor solvent. While the pristine P3HT film exhibited an enhancement factor of only 94 for methylene blue, the crystalline polymer films showed a significantly increased enhancement factor of 848. The P3HT-based SERS substrate demonstrated excellent signal reproducibility and long-term stability. Computational analysis revealed that strong π-interactions within the crystalline P3HT and with the methylene blue analyte molecules facilitated the chemical enhancement mechanism. Based on the calculated band gaps of the thiophene π-core (TP) and the MB-TP charge transfer complex (2.299 eV *vs.* 0.845 eV, respectively), a plausible charge transfer process from the HOMO of P3HT to the LUMO of MB seemed feasible upon laser excitation, enhancing the Raman signals. In the same year, Xu *et al.* reported a reusable organic–inorganic semiconductor heterojunction SERS platform based on the P3HT polymer and Ag_2NCN inorganic semiconductors.[131] The substrates were prepared by spin coating a chloroform solution of P3HT/Ag_2NCN, followed by immersion of the resulting film in a mixed solvent system to regulate the crystallization process. In designing this SERS platform, although $[NCN]^{2-}$ is electrically similar to the O^{2-} anion in metal oxides (*e.g.*, Ag_2O), its 2p orbitals create a higher valence band energy level, decreasing the band gap and enhancing the charge transfer processes. When the authors studied the SERS performance of the new P3HT-Ag2NCN hybrid substrate with methylene blue, they achieved an enhancement factor of 6147 and a detection limit value of 10^{-8} M. This represents a 7–75× enhancement in Raman signal amplification compared to either pristine P3HT or Ag_2NCN-nanorods.

In 2022, Rice *et al.* developed a bioinspired peptide-based SERS platform that enhanced Raman signals of varied analytes through an annealing-induced structural transition.[132] They used diphenylalanine peptide nanotubes (FFNTs) and prepared their substrates by drop-casting on glass followed by thermal annealing at temperatures of 100–200 °C. As the temperature increased from room temperature to 150 °C, the hollow hexagonal FFNTs transformed into closed fiber-like structures. The highest Raman enhancement factor (∼7×) was achieved with methylene blue on FFNTs annealed at 150 °C, with a low detection limit value of 10^{-7} M (Fig. 12). The enhancement was attributed to the increased surface area on the FFNT platform upon thermal annealing and the formation of new electronic states below the conduction band, which provided efficient pathways for charge transfer interactions between FFNT and analyte molecules. Photoluminescence decay profiles of the annealed and pristine FFNTs revealed that charge transfer resulted in longer analyte lifetimes. Additionally, the FFNT template enabled the detection of several mononucleotides (*i.e.*, thymine, uracil, and cytosine) at a concentration of 10^{-5} M. This study demonstrated the potential applications of peptide-based SERS platforms in biomedical fields, where chemical sensitivity is achieved through charge transfer.

3.3. Covalent organic framework-based SERS platforms

After reviewing the recent advances in polymer-based SERS-active substrates, we now turn our attention to another class of extended molecular systems: covalent organic frameworks (COFs). These compounds have recently gained attention as SERS-active substrates. COFs are crystalline organic polymers characterized by their highly ordered two- or three-dimensional porous structures.[155] The versatility of building block structures and covalent bonds formed between them enable great

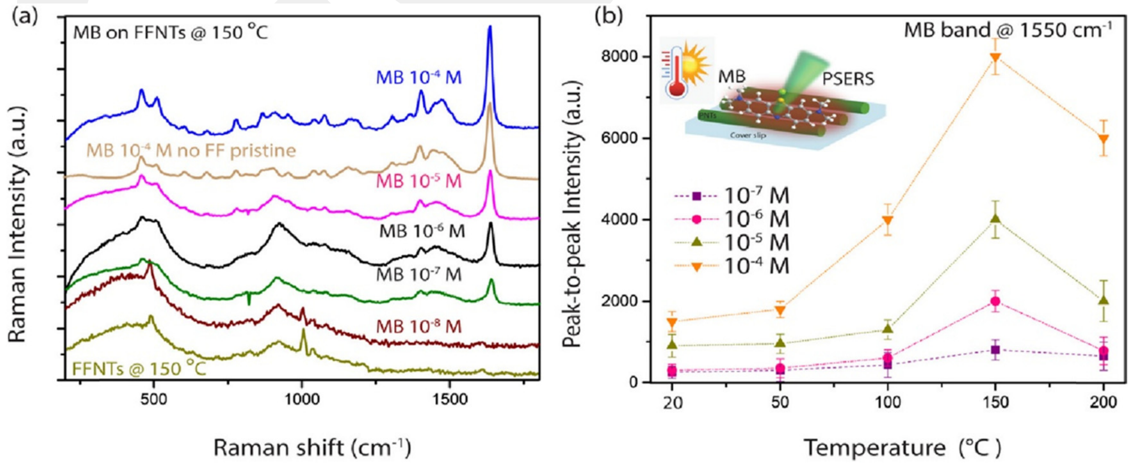

Fig. 12 (a) SERS spectra of methylene blue (MB) at concentrations ranging from 10^{-4} M to 10^{-8} M on FFNTs annealed at 150 °C, with a detection limit value of 10^{-7} M. The spectra of annealed FFNTs at 150 °C without MB are also included. (b) Graph showing the relative scattering intensity of MB at 1550 cm^{-1} as a function of temperature for various MB concentrations.[132] Reprinted with permission from ref. 132 Copyright 2022, American Chemical Society.

structural and topological diversity in COFs, making them suitable for tailor-made SERS platforms. COF structures can be designed with well-defined pore sizes, chemical structures, functional groups, and topologies. The high surface area and pore functionalization are particularly advantageous for SERS because they provide a large and efficient adsorption–chemisorption area for analytes and secondary SERS-active structures such as metallic nanoparticles. Although progress in COFs has been significant over the past two decades in various fields of materials science and nanotechnology, their application in SERS is still emerging, with only a limited number of reports, as described below.

In 2024, Kong and co-workers demonstrated significant SERS performance using a carbazole-based triazine COF compound (CTF-Cz).[133] This framework was synthesized *via* a superacid-catalyzed trimerization reaction and it showed a BET surface area of 117.3 $m^2\ g^{-1}$. CTF-Cz efficiently adsorbed R6G analyte molecules on its nanoporous (2–5 nm pore sizes) surface, relying on its strongly polar triazine units, yielding an enhancement factor of $\sim 10^5$ for the R6G analyte molecule. The LUMO energy level of CTF-Cz was recorded as -3.93 eV by electrochemistry, which is ~ 0.5 eV lower than that of the R6G analyte. This facilitates an energetically feasible charge transfer from R6G's HOMO to CTF-Cz's LUMO under the excitation wavelength of a 532 nm laser (2.33 eV). The authors note that while it is possible to excite R6G with the incident laser beam, it is not possible to excite CTF-Cz due to its wide band gap (3.13 eV). Therefore, molecular exciton only on the analyte molecule might be the other key contributor to the chemical enhancement mechanism. The charge transfer process was confirmed by time-resolved photoluminescence measurements. R6G on CTF-Cz exhibited a changed photoluminescence decay profile with two lifetimes of 0.76 ns and 4.76 ns, while pristine R6G on a silicon wafer showed a mono-exponential decay profile with a lifetime of 3.48 ns. Based on the experimental results, strong π-interactions, low LUMO level of the covalent framework, large delocalization of molecular orbitals, and effective adsorption of the analyte molecules due to the high surface area of the COF induce charge transfer interactions, ultimately increasing the Raman signal intensity.

Another key direction for COF compounds in SERS applications is the formation of COF-metal hybrid structures. Based on their unique porous structures with functional groups, COFs can act as scaffolds to stabilize noble metal nanoparticles, thereby facilitating the creation of SERS-active hot spots. In 2024, Fu *et al.* developed a hybrid TPDH-COF/Au-NPs SERS-active substrate.[134] The COF structure was synthesized by a Schiff base reaction, resulting in pores decorated with imine functional groups. The Au nanoparticles are stabilized on the COF structure *via* an electrostatic self-assembly method, forming a ''raspberry-like'' structure. Herein, electrostatic interactions between negatively charged gold nanoparticles and imine functional groups with positive charges contributed to the formation of SERS-active hot spots. While no Raman enhancement was observed on the pristine COF structure, TPDH-COF/Au-NPs showed an enhancement factor of 2.01×10^8 with R6G analyte molecules. Additionally, the authors tested their SERS platform with a pesticide molecule, thiabendazole (TBZ), which was detected at concentrations as low as ~ 5 ppb in a fruit juice. Although the authors mention a possible chemical enhancement mechanism, direct evidence was not demonstrated. Another example of utilizing a COF structure with Au-NPs was demonstrated in 2022 by Li and Chen *et al.*[135] In this case, a reversible SERS-based nanosensor, AuNPs@2-MBQ@COFs, was developed to dynamically monitor the redox processes in living cells. A redox-responsive Raman reporter molecule, 2-mercaptobenzoquinone (2-MBQ), was deposited on the Au-NP surface, which was then coated with a COF-shell structure *in situ* by using aldimine condensation reactions (Fig. 13). The incorporation of 2-MBQ allowed for the monitoring of redox dynamics in a living cell due to its reversible reduction and oxidation properties. The primary function of the COF shell structure was to provide stability and anti-interference capability, thereby enabling reliable monitoring of intracellular redox dynamics. This study sheds light on SERS-based nanosensors integrating COFs and their potential applications in living cells for monitoring the redox state of various processes, including physiology and pathology.

The functional groups on COF structures can stabilize metallic nanoparticles on their surfaces and induce selective intermolecular interactions with desired analyte molecules. In 2023, Chen *et al.* synthesized a carboxyl-functionalized SERS substrate, Ag-COF-COOH, to selectively detect melamine in milk.[136] The pore size and functional groups on the COF surface enabled molecule-specific sensing in the presence of other interferents in milk. Ag-COF-COOH displayed an enhancement factor of 2.49×10^8 with a detection limit value of 10^{-9} M for melamine. While the electromagnetic enhancement is attributed to the framework structure of the SERS platform, which enables the formation of highly ordered Ag-NPs with hot spots, the authors claimed that chemical enhancement results from charge transfer interactions between melamine and COF functional groups. Similarly, a phenanthroline (PA)-functionalized COF structure was reported by Xu *et al.* to stabilize silver nanoparticles (Ag-NPs).[137] The SERS platform, PA-COF-AgNPs, was synthesized *via in situ* growth of Ag-NPs in the COF structure, and the composite structure formation was based on coordination interactions between the phenanthroline's nitrogen atoms and Ag^+ ions. In the presence of Hg^{2+}, PA-COF-AgNPs can oxidize 3,3′,5,5′-tetramethylbenzidine (TMB) to *ox*-TMB due to the formation of silver amalgam on the surface of nanoparticles, leading to significant SERS enhancements. In this study, a triple-readout (colorimetry/fluorescence/SERS) strategy for Hg^{2+} was developed with high sensitivity and favorable selectivity, and the limit of detection value was reported to be as low as $\sim 2 \times 10^{-5}$ μM.

In addition to the studies reviewed herein, it is worth noting that several additional studies conducted in recent years have focused on metal-COF hybrid SERS-active structures. These studies have successfully detected both common analyte molecules and biological or food-related molecules such as thiram residues (in fruit juice), benzoic acid (in dairy products), and

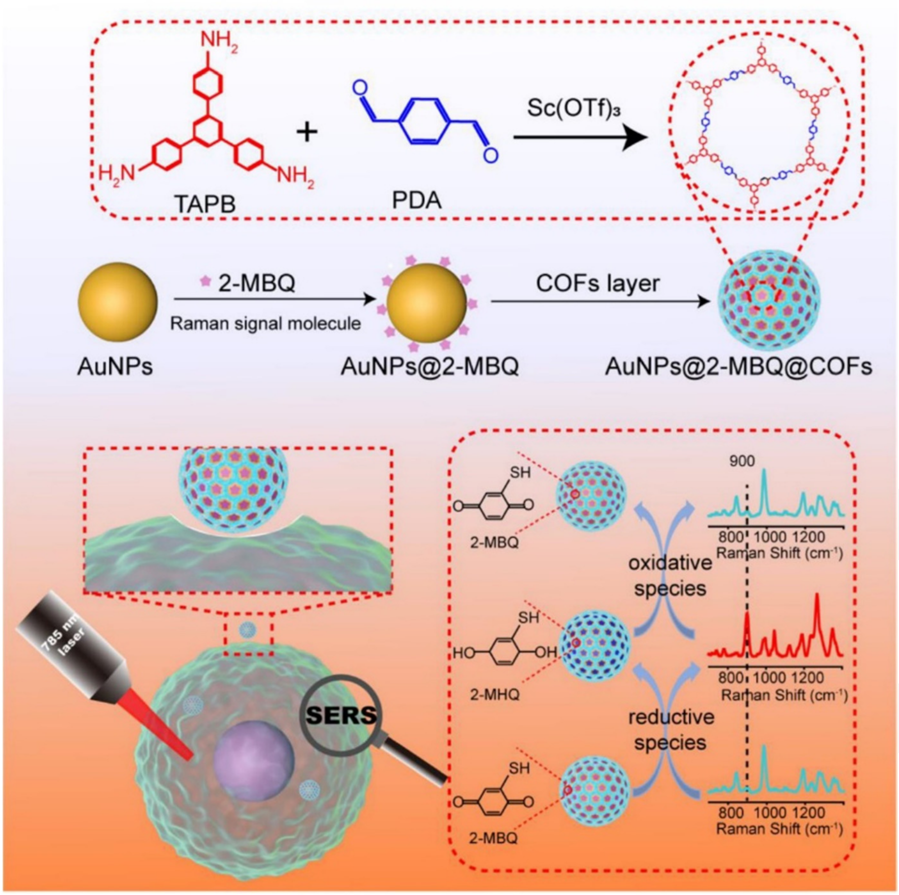

Fig. 13 Illustration of redox process monitoring in living cells using an AuNPs@2-MBQ@COFs Nanosensor.[135] Reprinted with permission from ref. 135 Copyright 2022, American Chemical Society.

estradiol using metal-COF SERS substrates.[138–141,156–158] At this point, it is crucial to highlight the scarcity of SERS studies having pristine COF structures as compared to COF–metal hybrid structures. Therefore, it is very important to allocate equal attention to exploring this avenue, especially by using diverse donor- and acceptor-type π-conjugated building blocks in COFs.

3.4. Graphene and 0D–3D carbon structure-based SERS platforms

Graphene is a two-dimensional honeycomb lattice composed of sp^2-hybridized carbon atoms, forming an extended one-atom-thick π-system. Since its discovery in 2004, graphene has garnered significant attention for its exceptional mechanical, (opto)electronic, spectroscopic, and chemical properties.[159] Alongside the polymers and covalent organic frameworks reviewed in the previous sections, single-to-few-layered graphene presents a unique π-extended system suitable for SERS applications.[160] Notably, it was the first carbon-based material with a noticeable Raman enhancement, as reported in 2010.[88] The use of a two-dimensional, atomically flat surface of graphene for the Raman enhancement is specifically called graphene-enhanced Raman scattering (GERS). Because plasmon resonances for graphene fall within the terahertz and mid-infrared ranges (rather than the visible range),[160–162] the chemical enhancement mechanism is regarded as the primary contributor to Raman enhancement on pristine graphene-based platforms, as reviewed herein. The Raman enhancement on the graphene surface stems from strong charge-transfer interactions between the extended graphene surface and the adsorbed/chemisorbed probe molecules, ultimately enhancing the polarizability derivative tensor of the analyte vibrational modes. Most importantly, atomically flat and defect-free graphene surfaces can enable quantitative analysis by preventing heterogeneous analyte adsorption and surface-related enhancement fluctuations. Additionally, when desired, graphene surfaces can be functionalized with various polar groups having heteroatoms, allowing for analyte-specific interactions and fine-tuning of analyte-surface interactions through electronic polarization effects.

Prior to the first-ever report on the SERS activity of graphene surfaces in 2010,[88] Zhang and Liu *et al.* discovered in 2009 that photoluminescence of fluorescent molecules, such as rhodamine 6G (R6G) and protoporphyrin IX (PPP), was quenched by 1000× upon adsorption on graphene during a resonance Raman spectroscopy (RRS) measurement.[163] This quenching enabled the achievement of clear Raman signals using the RRS technique. After obtaining the first evidence of feasible charge- and energy-transfers between small molecules and the graphene surface, the same research group demonstrated that mono- and few-layered graphene supported on Si–SiO$_2$ (300 nm) substrates could actually enhance the Raman signals of various adsorbed molecules.[88] In this study, the researchers applied several common probe molecules, such as phthalocyanine (Pc), rhodamine 6G (R6G), protoporphyrin IX (PPP), and crystal violet (CV). They utilized vacuum evaporation and solution-soaking methods for the submonolayer deposition of analytes, demonstrating the versatility of their GERS substrate. Enhanced Raman signal intensities were observed on the graphene monolayers, with enhancement factors ranging from 2 to 17 compared to the pristine Si–SiO$_2$ (300 nm) substrates. The detection limit values were as low as 10^{-8}–10^{-10} M for solution-soaked analytes. The π-stacked analyte molecules in direct contact with the graphene surface, with their HOMO–LUMO molecular energy levels positioned on either side of the Fermi level of graphene, are favorable for the chemical enhancement mechanism. The authors also found that increasing the number of graphene layers (from monolayers to multilayers/graphite) on top of the silicon substrate leads to reduced Raman signal intensity. This was attributed to the alterations in the electronic structures and the alignment of energy bands with analyte molecules as the number of graphene layers varied.[164] Further studies during the same years have shown that GERS is a first-layer effect and the increased number of graphene layers decreases the enhancement effect.[165,166] In the first phenomenon, the Raman enhancement on graphene is highly influenced by the distance between the analyte and the graphene surface, as well as the orientation of the analyte molecules (face-on *vs.* edge-on).[167] A separate study in 2011 demonstrated that the Raman enhancements of metal phthalocyanine (M-Pc) analytes on graphene could be modulated by changing the graphene Fermi level *via* the electrical field effect.[168] In this study, the modulation was found to be the strongest for the first-layer of analytes on a single layer of graphene. Some other additional studies in 2012–2013 have focused on using graphene to coat metallic (nano)structures to provide passivated, yet still active for electromagnetic enhancements, SERS substrates.[169,170] This way, the sensitivity and reproducibility of metallic-based SERS substrates have been improved. Although initial studies on GERS were based on pristine graphene-based substrates, Nam *et al.* in 2011 developed a p-doped graphene substrate containing oxygen-containing functional groups *via* UV/ozone-based oxidation methods.[109] Enhancement factors as large as $\sim 10^4$ were recorded over a centimeter-scale doped-/functionalized-graphene surface. On the other hand, strong molecular selectivity was demonstrated for the GERS effect, with enhancement factors varying by as much as two orders of magnitude depending on the specific analyte molecule.[171] The molecular energy levels (HOMO–LUMO energies of the analyte molecule *vs.* graphene's Fermi level) and the structural symmetry/substituents of the analyte molecules were found to be crucial in determining this molecular specificity during chemical enhancement effects. Feng *et al.* in 2016 developed a GERS platform based on nitrogen-doped monolayer graphene to detect very low concentrations of dye molecules: rhodamine B, crystal violet, and methylene blue.[90] The nitrogen-doped monolayer graphene was prepared on Cu foils using the ambient-pressure chemical vapor deposition method. The nitrogen doping level and configuration within the graphene lattice were controlled by varying the conditions of ammonia (NH$_3$) precursor introduction during synthesis. The nitrogen-doped graphene displayed enhanced GERS performance over pristine graphene (enhancement factor ≈ 2–16), owing to a significant charge transfer process resulting from its advantageous electronic structure. Dispersion-corrected DFT calculations demonstrated that doping causes the Fermi level (E_F) to shift and align with the lowest unoccupied molecular orbital (LUMO) energy level of the analyte molecule, consequently leading to an increased Raman signal intensity for specific vibrational modes (Fig. 14). The nitrogen-doped graphene substrate demonstrated an impressively low detection limit value of 10^{-11} M for all three analyte molecules. Furthermore, this substrate effectively detected the HOMO–LUMO gap of analyte molecules in resonant Raman measurements using different laser excitations.

While three-dimensional graphene retains many intrinsic features of two-dimensional graphene, it stands out due to its numerous adsorption sites for analyte molecules. This is because it has exposed atomically thin edges, which offer rapid electron transfer kinetics and large electroactive surface areas. Additionally, three-dimensional graphene features a distinctive resonant cavity structure that significantly enhances its light absorption capabilities. In 2022, Wang and colleagues designed a heterojunction SERS platform (3D-/2D-graphene/Ge) composed of two- and three-dimensional graphenes on a Ge substrate. The platform was fabricated using a plasma-assisted chemical vapor deposition method,[91] in which 2D-graphene was employed as the template layer for the growth of 3D-graphene. This way, the formation of an amorphous carbon layer beneath the 3D-graphene was effectively prevented, and the interaction and photo-induced charge transfer abilities of the 3D-graphene/Ge heterojunction were improved. The 3D-/2D-graphene/Ge heterojunction substrate utilized both chemical and electromagnetic enhancements simultaneously. Excellent linearity of the Raman signal intensity was observed with variations in analyte concentrations under 532 nm laser excitation. The SERS activity exhibited by the 3D-/2D graphene/Ge substrate enabled the authors to quantify the concentration of trace analyte molecules such as rhodamine 6G (R6G), rhodamine B (RB), methylene blue (MB), 3-hydroxytyramine hydrochloride (3-Hydro), and melamine (Mel). The limit of detection values were $\sim 10^{-10}$–10^{-8} M for the analyte molecules and less than 1 ppm for 3-Hydro and Mel compounds present in milk. In another recent study, Wang and co-workers developed a highly sensitive, three-dimensional (3D) hybrid heterogeneous SERS platform based on graphene nanostructures.[142] In their study, the authors decorated silver nanoparticles (Ag-NPs) and

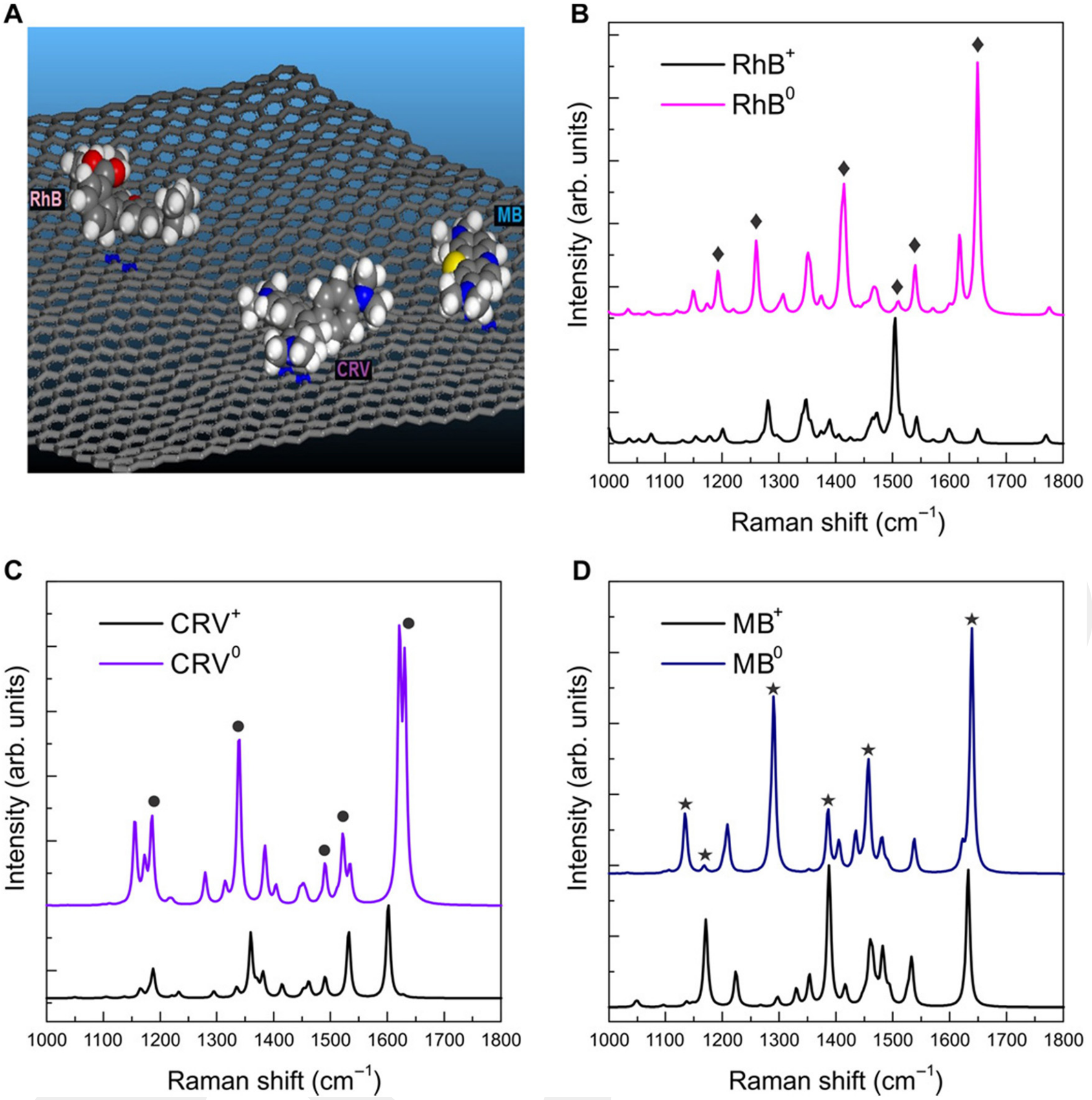

Fig. 14 Simulated configurations (a) and Raman spectra (b)–(d) of RhB, CRV, and MB analyte molecules (black curves for the cations and colored curves for the neutral molecules) on a nitrogen-doped graphene sheet.[90] Reprinted with permission from ref. 90 Copyright 2016, American Association for the Advancement of Science (AAAS).

graphene quantum dots (GQDs) (∼10 nm in diameter) onto 3D-graphene that was grown on a Si substrate. This Ag-NPs/GQDs/3D-graphene/Si SERS platform was used to detect different probe molecules such as rhodamine 6G (R6G), methylene blue (MB), dopamine (DA), and methyl parathion (MP)/tetramethylthiuram disulfide (TMTD), reaching remarkably low detection limits of 10^{-7}–10^{-11} M. Here, the detection of DA in deionized water and MP/TMTD in apple juice has demonstrated the potential utility of the Ag-NPs/GQDs/3D-graphene/Si SERS substrate in applications related to food safety and water science. Finite-difference time-domain (FDTD) calculations and scanning Kelvin probe microscopy (SKPM) measurements unveiled the underlying reasons for the observed SERS performance, which was attributed to the presence of both electromagnetic (*i.e.*, hot spot formation in Ag-NPs) and chemical enhancement (*i.e.*, in the GQDs/3D-graphene/Si heterojunction) mechanisms.

Graphene oxide and its reduced form are two graphene-based structures that possess a certain degree of oxygen-containing surface polar functionalizations. In one of the early studies, Luo and Wang *et al.* demonstrated that mildly reduced graphene oxide (MR-GO) nanosheets could exhibit improved enhancement factors (10×) compared to pristine graphene.[110] This improvement is attributed to the strong local electric fields created by electronegative oxygen species. Very recently, Ramírez-García *et al.* developed a sensitive hybrid SERS substrate composed of graphene oxide (GO) and quantum-sized ZrO_2 nanoparticles for the detection of methyl parathion (MP) pesticide in water bodies, as well as in strawberry and black tea extracts.[75] The GO/ZrO_2 substrate demonstrated a SERS

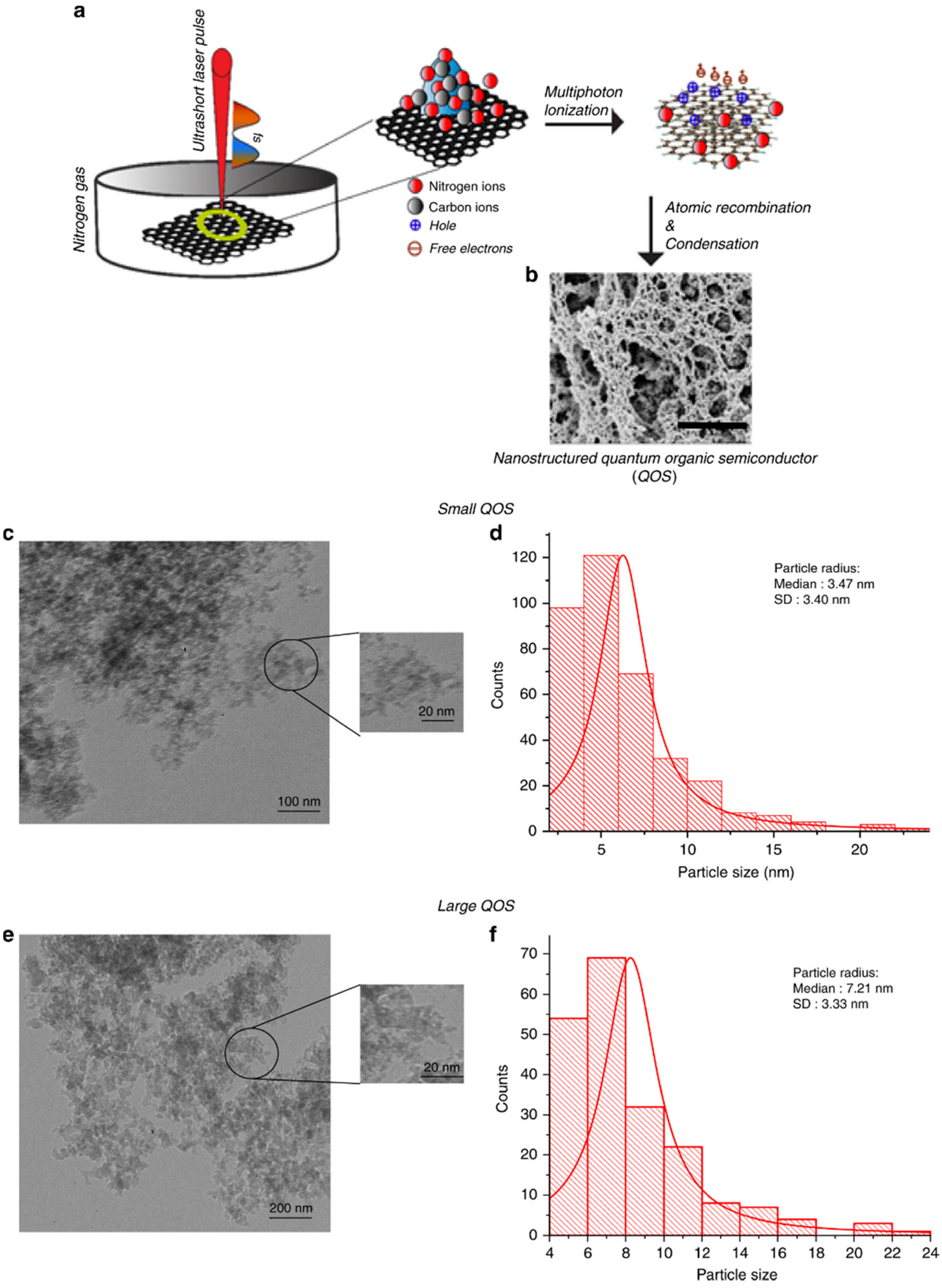

Fig. 15 (a) Synthesis of quantum organic semiconductors (QOS) using a femtosecond laser pulse in a low-pressure nitrogen atmosphere. The top-view scanning electron microscopy image (b) displaying interconnected QOS probes and the morphology of small QOS (c) and large QOS (e) with their corresponding size distributions (d and f, respectively).[150] Reprinted with permission from ref. 150 Copyright 2020, Springer Nature.

enhancement factor of 8.78×10^4 with a detection limit value of 0.12 μM, which is more than five times more efficient than that of the pristine ZrO_2 substrate. This indicates the significant effect of the graphene oxide substrate in Raman enhancement, and the improvement originated from the reduced charge recombination due to the transfer of photoinduced holes in the ZrO_2 nanoparticles to the graphene oxide (GO) layer. In the same year, Tran and Phan *et al.* introduced another hybrid SERS platform integrating multilayer reduced graphene oxide (rGO) with silver nanoparticles to enhance the Raman signal intensity through both chemical and electromagnetic mechanisms. The rGO/Ag-NP substrate was prepared by immersing glass/rGO films into Ag-NP solutions for several hours, which showed a large enhancement factor of $\sim 10^8$ and a low detection limit value of 10^{-9} M for methylene blue.[151] The SERS performance of rGO/Ag-NPs was found to be superior to four other structures: Ag-NPs, Ag thin films, Ag thin films/Ag-NPs, and Ag thin films/Au-NPs. Minh *et al.* unveiled the additional properties of graphene in SERS applications beyond signal enhancement and enhanced adsorption.[143] They utilized a unique fabrication sequence for the SERS substrate, initially depositing silver nanoparticles on a cotton Q-tip, followed by covering them with a thin layer of graphene oxide (GO) using dip-coating. The GO/AgNPs/cotton swab substrate demonstrated an enhancement factor of 3–5 $\times 10^{10}$ and a detection limit value of 10^{-10} M for Rhodamine B. This approach allowed the authors to protect the silver nanoparticles from degradation by using GO as a barrier against the ambient atmosphere, resulting in the development of a SERS platform with an efficient sample collection method. In a very recent study reported in 2024, Chen and Jung *et al.* demonstrated that the introduction of an Ag-reduced graphene oxide (rGO) structure into a poly(3,4- ethylenedioxythiophene):poly(styrene sulfonate) (PEDOT:PSS) film enhanced the electromagnetic field effect and improved the analyte–polymer substrate interactions for SERS detection.[144] This study opens up new possibilities for developing graphene–polymer hybrid SERS-active platforms. At this point, it is worth noting that over the past decade, there have been several additional reports on hybrid SERS platforms that integrate reduced graphene oxide (rGO) and silver nanoparticles or nanodendrites.[145,146]

As an example of a two-dimensional graphitic structure, Amin *et al.* recently reported a graphitic carbon nitride (gCN)-based SERS platform. In this platform, gCN was functionalized with polymer brushes *via* surface-initiated photografting and photopolymerization (SIPGP).[147] The gCN structure was prepared from melamine by thermal oxidation etching in air, and the SIPGP method did not alter the original gCN structure. Polymer brush patterning on the gCN surface was achieved using photomask and microcontact printing techniques, which aimed to enhance the dispersibility of gCNs in common solvents, including water, ethanol, and tetrahydrofuran. After integrating Ag nanoparticles into the polymer brushes, the AgNPs/PDMAEMA-g-gCN hybrid structure exhibited strong SERS activity with an enhancement factor of 2.4×10^7 for the R6G analyte dye molecule. Additionally, the authors demonstrated the recyclable use of the same platform to remove R6G *via* photocatalytic degradation under visible light irradiation, making their platform a multifunctional sensing layer for both SERS and photocatalysis. As an example of a two-dimensional carbon-based nanostructured template in SERS, González-Domínguez *et al.* developed thiolated graphene oxide nanoribbons (GONRs) in 2019.[148] GONRs were synthesized through oxidative unzipping of multi-walled carbon nanotubes (MWCNTs), in which the length of the original structures was reduced, resulting in the formation of bidimensional flakes with sizes of 480 × 46 nm. In this study, the functionalization with terminal thiol groups fostered a strong interaction between GONRs and Au-NPs, which led to the formation of two-dimensional AuNP clusters with hot spots. The GONRs–AuNPs hybrid structure deposited on a glass substrate showed Raman enhancements for crystal violet analyte molecules.

The early report on a graphene-based quantum structure was in 2018 by Wei *et al.* They synthesized highly crystalline, atomically clean graphene quantum dots (GQDs) (down to 2 nm sizes) directly on a Si/SiO_2 substrate by using a quasi-equilibrium plasma-enhanced chemical vapor deposition method.[149] Enhancement factors greater than 10^3 and detection limit values as low as 10^{-9} M (with R6G) were achieved and attributed to enhanced charge transfer interactions between the analyte molecules and GQDs. As another example of a carbon-based quantum structure, a nanostructured quantum organic semiconductor (QOS)-based SERS platform, was developed by Venkatakrishnan *et al.* in 2020 for tag-free genomic DNA detection.[150] Genomic DNA contains crucial information about structural, molecular, and genetic modifications, which can serve as effective markers for cancer stem cells. In this study, the utilization of ultrashort pulsed laser processing on graphite in the presence of nitrogen gas allowed the miniaturization of the organic semiconductor down to the quantum scale ($\sim$3–7 nm) (Fig. 15). This process led to enhancements in the charge carrier mobility and the surface area for molecular adsorption, which are both crucial for facilitating efficient charge transfer interactions for SERS. Reducing the organic semiconductor to a smaller scale enhanced the SERS sensitivity to a single molecule level. QOS-based substrates exhibited the impressive SERS performance with a large enhancement factor of 10^{12} and femtomole sensitivity for crystal violet and rhodamine 6G. This study showed that quantum-scale organic semiconductors hold great promise as a novel label-free tool for single-molecule genomic DNA sensing.

4. Conclusions

In this review, we cover recent advancements in the development of SERS-active substrates, specifically highlighting unique inorganic- and organic-based materials that have been employed with notable Raman enhancements and clear enhancement mechanisms (Table 1 and 2). Over the past few decades, we have seen significant achievements in the development of new SERS platforms with innovative and effective (in)organic materials. Bridging the gap between Raman spectroscopy and materials science, SERS opens doors to fascinating possibilities, not only by creating new SERS-active materials but also by applying them to various real-life applications. Notably, in the last decade, the SERS field has shifted its focus from traditional plasmonic surfaces, such as Au and Ag, which rely on a universal electromagnetic enhancement mechanism, to exploring novel inorganic and organic-based materials that utilize analyte-specific chemical enhancement effects. Since the 1970s, the electromagnetic enhancement, particularly for noble metals, has been thoroughly studied in various systems. Until the beginning of the last decade, it was extremely rare to find a SERS substrate that exhibited only chemical enhancement without any contribution from the electromagnetic enhancement. In this perspective, the inorganic and organic material families developed in recent decades offer new possibilities to become key players in the field of SERS. Despite the impressive advancements reviewed herein, deeper investigations and newer strategies are still essential to fully unlock the potential of semiconductor-based SERS technology. The origin and role of chemical enhancement are constantly under debate as it is a more complicated process than electromagnetic enhancement, and it typically involves varied pathways, including both the semiconductor's and analyte's electronic states/wave functions. In addition, the chemical enhancement mechanism is dependent on the analyte molecule, which is very different from the electromagnetic enhancement mechanism, and, thereby, it can be tuned to engineer interactions with varied analyte molecules, which brings its own challenges and opportunities. Most importantly, it will be possible to design molecule-specific SERS platforms in diverse real-life applications by tuning the (in)organic materials structure/composition, film morphology/microstructure, and electronic structure. The ability to detect multiple analytes simultaneously in a sample with controllable sensitivity would significantly enhance its utility in various fields. Each day, the versatility and use of (in)organics as SERS platforms continue to grow, with the specific goals of expanding and better understanding the utility of chemical enhancement in SERS. Although inorganic semiconductors offer unique possibilities for SERS applications, they still face some major challenges, including long-term stability, reproducibility, and high sensitivity. Furthermore, the search for appropriate inorganic semiconductors with unique HOMO–LUMO energy levels is certainly needed in order to reach their true potential for real-life SERS applications. Controlling the electronic properties of inorganic semiconductors to achieve optimal SERS enhancement still remains a challenge. This limits the ability to fine tune the inorganic semiconductor materials for specific target molecules. On the other hand, the structural versatility of organic SERS materials is particularly advantageous, as exploratory synthesis can lead to the development of an unlimited variety of organic π-systems. Some (in)organic semiconductors can also degrade over time, especially under the exposure of light. This can lead to inconsistent field enhancement in SERS and hinder their practical applications. Developing cost-effective and scalable fabrication methods for high-quality inorganic SERS substrates can also be difficult, limiting their widespread adoption and integration into real-life applications. In addition to these, some inorganic semiconductors might not be biocompatible, restricting their use in biological and medical SERS applications where interaction with living tissues is necessary. In terms of biocompatibility, scalability, and cost-effective platform fabrication, organic materials could offer more advantages. As a future development perspective, the formation of free charge carriers on the organic π-systems *via* (electro)chemical doping or donor–acceptor type conductive electronic structure designs and electromagnetic enhancement could be a strong alternative for Raman enhancement in the near future. Overall, SERS, which is based on organic and inorganic materials, has the potential to revolutionize various scientific and technological fields. Especially, developing cost-effective and scalable fabrication methods with organic materials could open doors to numerous practical SERS detection applications that are not feasible now. The future of SERS-active (in)organic materials holds promise for more sensitive, selective, and versatile SERS platforms, potentially leading to ground-breaking advancements in healthcare, environmental monitoring, food safety, and advanced materials development.

Data availability

No primary research results, software, or code have been included, and no new data were generated or analyzed as part of this review.

Conflicts of interest

There are no conflicts to declare.

Acknowledgements

G. D. acknowledges support from the Gazi University grant number FBG-2022-7884.

References

1 P. L. Stiles, J. A. Dieringer, N. C. Shah and R. P. Van Duyne, *Annu. Rev. Anal. Chem.*, 2008, **1**, 601–626.

2 J. Langer, D. Jimenez de Aberasturi, J. Aizpurua, R. A. Alvarez-Puebla, B. Auguié, J. J. Baumberg, G. C. Bazan, S. E. J. Bell, A. Boisen, A. G. Brolo, J. Choo, D. Cialla-May, V. Deckert, L. Fabris, K. Faulds, F. J. García de Abajo, R. Goodacre, D. Graham, A. J. Haes, C. L. Haynes, C. Huck, T. Itoh, M. Käll, J. Kneipp, N. A. Kotov, H. Kuang, E. C. Le Ru, H. K. Lee, J.-F. Li, X. Y. Ling, S. A. Maier, T. Mayerhöfer, M. Moskovits, K. Murakoshi, J.-M. Nam, S. Nie, Y. Ozaki, I. Pastoriza-Santos, J. Perez-Juste, J. Popp, A. Pucci, S. Reich, B. Ren, G. C. Schatz, T. Shegai, S. Schlücker, L.-L. Tay, K. G. Thomas, Z.-Q. Tian, R. P. Van Duyne, T. Vo-Dinh, Y. Wang, K. A. Willets, C. Xu, H. Xu, Y. Xu,

Y. S. Yamamoto, B. Zhao and L. M. Liz-Marzán, *ACS Nano*, 2020, **14**, 28–117.
3 A. Campion and P. Kambhampati, *Chem. Soc. Rev.*, 1998, **27**, 241–250.
4 X. X. Han, R. S. Rodriguez, C. L. Haynes, Y. Ozaki and B. Zhao, *Nat. Rev. Methods Primers*, 2022, **1**, 87.
5 G. Demirel, H. Usta, M. Yilmaz, M. Celik, H. A. Alidagi and F. Buyukserin, *J. Mater. Chem. C*, 2018, **6**, 5314–5335.
6 Y. Yang, S. Wu, Y. Chen and H. Ju, *Chem. Sci.*, 2023, **14**, 12869–12882.
7 C. Hess, *Chem. Soc. Rev.*, 2021, **50**, 3519–3564.
8 Y. Hang, J. Boryczka and N. Wu, *Chem. Soc. Rev.*, 2022, **51**, 329–375.
9 Y. Huo, Z. Yang, T. Wilson and C. Jiang, *Adv. Mater. Interfaces*, 2022, **9**, 2200201.
10 M. Fleischmann, P. J. Hendra and A. J. McQuillan, *Chem. Phys. Lett.*, 1974, **26**, 163–166.
11 H.-L. Wang, E.-M. You, R. Panneerselvam, S.-Y. Ding and Z.-Q. Tian, *Light: Sci. Appl.*, 2021, **10**, 161.
12 Y. Ying, Z. Tang and Y. Liu, *Nanoscale*, 2023, **15**, 10860–10881.
13 S.-Y. Ding, E.-M. You, Z.-Q. Tian and M. Moskovits, *Chem. Soc. Rev.*, 2017, **46**, 4042–4076.
14 L. Tong, T. Zhu and Z. Liu, *Chem. Soc. Rev.*, 2011, **40**, 1296–1304.
15 R. G. Freeman, K. C. Grabar, K. J. Allison, R. M. Bright, J. A. Davis, A. P. Guthrie, M. B. Hommer, M. A. Jackson, P. C. Smith, D. G. Walter and M. J. Natan, *Science*, 1995, **267**, 1629–1632.
16 A. Doron, E. Katz and I. Willner, *Langmuir*, 1995, **11**, 1313–1317.
17 P. Kambhampati, C. M. Child, M. C. Foster and A. Campion, *J. Chem. Phys.*, 1998, **108**, 5013–5026.
18 N. Valley, N. Greeneltch, R. P. Van Duyne and G. C. Schatz, *J. Phys. Chem. Lett.*, 2013, **4**, 2599–2604.
19 X. Wang, E. Zhang, H. Shi, Y. Tao and X. Ren, *Analyst*, 2022, **147**, 1257–1272.
20 X. X. Han, W. Ji, B. Zhao and Y. Ozaki, *Nanoscale*, 2017, **9**, 4847–4861.
21 J. R. Lombardi and R. L. Birke, *J. Phys. Chem. C*, 2014, **118**, 11120–11130.
22 S. Jin, D. Zhang, B. Yang, S. Guo, L. Chen and Y. M. Jung, *Analyst*, 2024, **149**, 11–28.
23 G. Song, S. Cong and Z. Zhao, *Chem. Sci.*, 2022, **13**, 1210–1224.
24 Q. Wang, K. Chang, Q. Yang and W. Wu, *Trends Food Sci. Technol.*, 2024, **147**, 104460.
25 H. Yamada, Y. Yamamoto and N. Tani, *Chem. Phys. Lett.*, 1982, **86**, 397–400.
26 H. Yamada and Y. Yamamoto, *Surf. Sci.*, 1983, **134**, 71–90.
27 B. Abraham, L. G. C. Rego and L. Gundlach, *J. Phys. Chem. C*, 2019, **123**, 23760–23772.
28 Y. Liu, H. Ma, X. X. Han and B. Zhao, *Mater. Horiz.*, 2021, **8**, 370–382.
29 J. R. Lombardi, *Faraday Discuss.*, 2017, **205**, 105–120.
30 Z. Zheng, S. Cong, W. Gong, J. Xuan, G. Li, W. Lu, F. Geng and Z. Zhao, *Nat. Commun.*, 2017, **8**, 1993.
31 S. Cong, Y. Yuan, Z. Chen, J. Hou, M. Yang, Y. Su, Y. Zhang, L. Li, Q. Li, F. Geng and Z. Zhao, *Nat. Commun.*, 2015, **6**, 7800.
32 J. R. Lombardi, R. L. Birke, T. Lu and J. Xu, *J. Chem. Phys.*, 1986, **84**, 4174–4180.
33 V. Rajput, R. K. Gupta and J. Prakash, *J. Mater. Chem. C*, 2022, **10**, 73–95.
34 H. Wu, H. Wang and G. Li, *Analyst*, 2017, **142**, 326–335.
35 X. Du, D. Liu, K. An, S. Jiang, Z. Wei, S. Wang, W. F. Ip and H. Pan, *Appl. Mater. Today*, 2022, **29**, 101563.
36 Y. Wang, W. Ruan, J. Zhang, B. Yang, W. Xu, B. Zhao and J. R. Lombardi, *J. Raman Spectrosc.*, 2009, **40**, 1072–1077.
37 L. Jiang, T. You, P. Yin, Y. Shang, D. Zhang, L. Guo and S. Yang, *Nanoscale*, 2013, **5**, 2784–2789.
38 Q. Q. Zhang, X. Li, Q. Ma, Q. Q. Zhang, H. Bai, W. Yi, J. Liu, J. Han and G. Xi, *Nat. Commun.*, 2017, **8**, 14903.
39 L. Tang, X. Pan, M. Luo, R. Yang, L. Guo, Z. Sun, S. Jiang, J. Jiang, G. Zhang and Q. Zhu, *J. Mater. Chem. A*, 2023, **11**, 16212–16220.
40 P. Miao, J. Wu, Y. Du, Y. Sun and P. Xu, *J. Mater. Chem. C*, 2018, **6**, 10855–10860.
41 X. Hou, X. Fan, P. Wei and T. Qiu, *J. Mater. Chem. C*, 2019, **7**, 11134–11141.
42 D. Büchel, C. Mihalcea, T. Fukaya, N. Atoda, J. Tominaga, T. Kikukawa and H. Fuji, *Appl. Phys. Lett.*, 2001, **79**, 620–622.
43 A. Musumeci, D. Gosztola, T. Schiller, N. M. Dimitrijevic, V. Mujica, D. Martin and T. Rajh, *J. Am. Chem. Soc.*, 2009, **131**, 6040–6041.
44 D. Qi, L. Lu, L. Wang and J. Zhang, *J. Am. Chem. Soc.*, 2014, **136**, 9886–9889.
45 Y. Dong, Q. Xie, S. Wu, J. Li, L. Sun and W. Ji, *J. Phys. Chem. C*, 2023, **127**, 9418–9424.
46 J. S. Teguh, F. Liu, B. Xing and E. K. L. Yeow, *Chem. – Asian J.*, 2012, **7**, 975–981.
47 J. Li, H. Zhang, D. Yu, W. Wang, W. Song, L. Yang, X. Jiang and B. Zhao, *Spectrochim. Acta, Part A*, 2022, **281**, 121643.
48 X. Wang, W. Shi, Z. Jin, W. Huang, J. Lin, G. Ma, S. Li and L. Guo, *Angew. Chem., Int. Ed.*, 2017, **56**, 9851–9855.
49 K. M. Arun Kumar, T. Kokulnathan, T.-J. Wang, A. Joseph Anthuvan, K.-J. Chen and Y.-H. Chang, *Appl. Surf. Sci.*, 2024, **660**, 160000.
50 J. Lin, Y. Shang, X. Li, J. Yu, X. Wang and L. Guo, *Adv. Mater.*, 2017, **29**, 1604797.
51 X. Zheng, F. Ren, S. Zhang, X. Zhang, H. Wu, X. Zhang, Z. Xing, W. Qin, Y. Liu and C. Jiang, *ACS Appl. Mater. Interfaces*, 2017, **9**, 14534–14544.
52 X. Song, Y. Wang, F. Zhao, Q. Li, H. Q. Ta, M. H. Rümmeli, C. G. Tully, Z. Li, W.-J. Yin, L. Yang, K.-B. Lee, J. Yang, I. Bozkurt, S. Liu, W. Zhang and M. Chhowalla, *ACS Nano*, 2019, **13**, 8312–8319.
53 X. Li, S. Ye and X. Luo, *Chem. Commun.*, 2016, **52**, 10269–10272.

54 Y. Wang, J. Zhang, H. Jia, M. Li, J. Zeng, B. Yang, B. Zhao, W. Xu and J. R. Lombardi, *J. Phys. Chem. C*, 2008, **112**, 996–1000.
55 L. Tao, K. Chen, Z. Chen, C. Cong, C. Qiu, J. Chen, X. Wang, H. Chen, T. Yu, W. Xie, S. Deng and J.-B. Xu, *J. Am. Chem. Soc.*, 2018, **140**, 8696–8704.
56 M. Shafi, M. Zhou, P. Duan, W. Liu, W. Zhang, Z. Zha, J. Gao, S. Wali, S. Jiang, B. Man and M. Liu, *Sens. Actuators, B*, 2022, **356**, 131360.
57 D. Rani, S. Patel, M. Austeria P, P. V. Babu and S. Sampath, *J. Phys. Chem. C*, 2023, **127**, 3131–3141.
58 X. Wang, W. Shi, G. She and L. Mu, *J. Am. Chem. Soc.*, 2011, **133**, 16518–16523.
59 A. Sarycheva, T. Makaryan, K. Maleski, E. Satheeshkumar, A. Melikyan, H. Minassian, M. Yoshimura and Y. Gogotsi, *J. Phys. Chem. C*, 2017, **121**, 19983–19988.
60 H. Sun, S. Cong, Z. Zheng, Z. Wang, Z. Chen and Z. Zhao, *J. Am. Chem. Soc.*, 2019, **141**, 870–878.
61 J. Wang, C. Qiu, H. Pang, J. Wu, M. Sun and D. Liu, *J. Mater. Chem. C*, 2021, **9**, 9011–9020.
62 X. Wang, W. Shi, S. Wang, H. Zhao, J. Lin, Z. Yang, M. Chen and L. Guo, *J. Am. Chem. Soc.*, 2019, **141**, 5856–5862.
63 H. Wu, X. Zhou, J. Li, X. Li, B. Li, W. Fei, J. Zhou, J. Yin and W. Guo, *Small*, 2018, **14**, 1802276.
64 H. Li, Q. Xu, X. Wang and W. Liu, *Small*, 2018, **14**, 20181523.
65 F. Li, X. Mu, X. Tang, G. Song, H. Sun, X. Zha, P. Sun, J. Fang, D. Hu, S. Cong and Z. Zhao, *Angew. Chem., Int. Ed.*, 2023, **62**, e202218055.
66 K. Li, H. Jiang, L. Wang, R. Wang, X. Zhang, L. Yang, X. Jiang, W. Song and B. Zhao, *Microchim. Acta*, 2024, **191**, 113.
67 H. Liu, Q. Li, Y. Ma, S. Wang, Y. Wang, B. Zhao, L. Zhao, Z. Jiang, L. Xu and W. Ruan, *Spectrochim. Acta, Part A*, 2023, **303**, 123168.
68 P. Ji, Z. Mao, Z. Wang, X. Xue, Y. Zhang, J. Lv and X. Shi, *Nanomaterials*, 2019, **9**, 983.
69 L. Yang, Y. Peng, Y. Yang, J. Liu, H. Huang, B. Yu, J. Zhao, Y. Lu, Z. Huang, Z. Li and J. R. Lombardi, *Adv. Sci.*, 2019, **6**, 1900310.
70 J. Zhang, Y. Pan, Y. Chen and H. Lu, *J. Mater. Chem. C*, 2018, **6**, 2216–2220.
71 X. Tan, L. Wang, C. Cheng, X. Yan, B. Shen and J. Zhang, *Chem. Commun.*, 2016, **52**, 2893–2896.
72 Y. Yang, D. Du, F. Kong, J. Fan and T. Qiu, *J. Appl. Phys.*, 2015, **117**, 245307.
73 X. Li, Y. Wu, Y. Shen, Y. Sun, Y. Yang and A. Xie, *Appl. Surf. Sci.*, 2018, **427**, 739–744.
74 R.-C. Wang, Y.-H. Chen, H.-H. Huang, K.-T. Lin, Y.-S. Jheng and C.-Y. Liu, *Appl. Surf. Sci.*, 2020, **521**, 146426.
75 M. Vargas-Zamarripa, A. A. Rivera, U. Sierra, P. Salas, A. H. Serafín-Muñoz and G. Ramírez-García, *Chemosphere*, 2023, **320**, 138081.
76 M. Liu, W. Liu, W. Zhang, P. Duan, M. Shafi, C. Zhang, X. Hu, G. Wang and W. Zhang, *ACS Appl. Mater. Interfaces*, 2022, **14**, 56975–56985.
77 J. P. Fraser, P. Postnikov, E. Miliutina, Z. Kolska, R. Valiev, V. Švorčík, O. Lyutakov, A. Y. Ganin and O. Guselnikova, *ACS Appl. Mater. Interfaces*, 2020, **12**, 47774–47783.
78 G. Kim, D. W. Jeong, G. Lee, S. Lee, K. Y. Ma, H. Hwang, S. Jang, J. Hong, S. Pak, S. Cha, D. Cho, S. Kim, J. Lim, Y. Lee, H. S. Shin, A. Jang and J. Lee, *Small*, 2024, **20**, 2306819.
79 K. An, M. Chen, B. He, H. Ai, W. Wang, Z. Zhang, Z. Pan, S. Chen, W. F. Ip, K. H. Lo, J. Chai, S. Wang, M. Yang, S. Wang and H. Pan, *Adv. Mater. Technol.*, 2022, **7**, 2200217.
80 J. Dong, J. Huang, A. Wang, G. V. Biesold-McGee, X. Zhang, S. Gao, S. Wang, Y. Lai and Z. Lin, *Nano Energy*, 2020, **71**, 104579.
81 A. Li, J. Lin, Z. Huang, X. Wang and L. Guo, *iScience*, 2018, **10**, 1–10.
82 X. Li, M. Su, Y.-C. Wang, M. Xu, M. Tong, S. J. Haigh and J. Zhang, *Inorg. Chem.*, 2022, **61**, 3989–3996.
83 Z. Lei, D. Wu, X. Cao, X. Zhang, L. Tao, Z. Zheng, X. Feng, L. Tao and Y. Zhao, *J. Alloys Compd.*, 2023, **937**, 168294.
84 P. Miao, J. Qin, Y. Shen, H. Su, J. Dai, B. Song, Y. Du, M. Sun, W. Zhang, H. Wang, C. Xu and P. Xu, *Small*, 2018, **14**, 1704079.
85 L. Quan, Y. Song, Y. Lin, G. Zhang, Y. Dai, Y. Wu, K. Jin, H. Ding, N. Pan, Y. Luo and X. Wang, *J. Mater. Chem. C*, 2015, **3**, 11129–11134.
86 C. Weng, Y. Luo, B. Wang, J. Shi, L. Gao, Z. Cao and G. Duan, *J. Mater. Chem. C*, 2020, **8**, 14138–14145.
87 R. Livingstone, X. Zhou, M. C. Tamargo, J. R. Lombardi, L. G. Quagliano and F. Jean-Mary, *J. Phys. Chem. C*, 2010, **114**, 17460–17464.
88 X. Ling, L. Xie, Y. Fang, H. Xu, H. Zhang, J. Kong, M. S. Dresselhaus, J. Zhang and Z. Liu, *Nano Lett.*, 2010, **10**, 553–561.
89 A. S. Matsukovich, O. Y. Nalivaiko, K. V. Chizh and S. V. Gaponenko, *J. Appl. Spectrosc.*, 2019, **86**, 72–75.
90 S. Feng, M. C. dos Santos, B. R. Carvalho, R. Lv, Q. Li, K. Fujisawa, A. L. Elías, Y. Lei, N. Perea-López, M. Endo, M. Pan, M. A. Pimenta and M. Terrones, *Sci. Adv.*, 2016, **2**, e1600322.
91 Z. He, L. Yu, G. Wang, C. Ye, X. Feng, L. Zheng, S. Yang, G. Zhang, G. Wei, Z. Liu, Z. Xue and G. Ding, *ACS Appl. Mater. Interfaces*, 2022, **14**, 14764–14773.
92 Y. Gao, N. Gao, H. Li, X. Yuan, Q. Wang, S. Cheng and J. Liu, *Nanoscale*, 2018, **10**, 15788–15792.
93 X. Li, J. Yang, F. Ye, L. Xiao, X. Li, J. Weng and L. Sun, *ACS Appl. Nano Mater.*, 2024, **7**, 2291–2303.
94 J. Xu, C. Cheng, S. Shang, W. Gao, P. Zeng and S. Jiang, *ACS Appl. Mater. Interfaces*, 2020, **12**, 49452–49463.
95 X. Chen, L. Qin, S.-Z. Kang and X. Li, *Appl. Surf. Sci.*, 2021, **550**, 149302.
96 T. B. Limbu, B. Chitara, J. D. Orlando, M. Y. Garcia Cervantes, S. Kumari, Q. Li, Y. Tang and F. Yan, *J. Mater. Chem. C*, 2020, **8**, 4722–4731.
97 B. Soundiraraju and B. K. George, *ACS Nano*, 2017, **11**, 8892–8900.
98 L. G. Quagliano, *J. Am. Chem. Soc.*, 2004, **126**, 7393–7398.

99 Z. Li, L. Zhai, Q. Zhang, W. Zhai, P. Li, B. Chen, C. Chen, Y. Yao, Y. Ge, H. Yang, P. Qiao, J. Kang, Z. Shi, A. Zhang, H. Wang, J. Liang, J. Liu, Z. Guan, L. Liao, V. A. Neacşu, C. Ma, Y. Chen, Y. Zhu, C.-S. Lee, L. Ma, Y. Du, L. Gu, J.-F. Li, Z.-Q. Tian, F. Ding and H. Zhang, *Nat. Mater.*, DOI: 10.1038/s41563-024-01860-w.

100 E. Er, H.-L. Hou, A. Criado, J. Langer, M. Möller, N. Erk, L. M. Liz-Marzán and M. Prato, *Chem. Mater.*, 2019, **31**, 5725–5734.

101 M.-R. Gao, Y.-F. Xu, J. Jiang and S.-H. Yu, *Chem. Soc. Rev.*, 2013, **42**, 2986–3017.

102 H. Lai, G. Li, F. Xu and Z. Zhang, *J. Mater. Chem. C*, 2020, **8**, 2952–2963.

103 C. Huang, A. Li, X. Chen and T. Wang, *Small*, 2020, **16**, 2004802.

104 Z. Jiang, P. Gao, L. Yang, C. Huang and Y. Li, *Anal. Chem.*, 2015, **87**, 12177–12182.

105 T. Yu, C. Ho, C. Wu, C. Chien, C. Lin and S. Lee, *J. Raman Spectrosc.*, 2013, **44**, 1506–1511.

106 J. Fu, Z. Zhong, D. Xie, Y. Guo, D. Kong, Z. Zhao, Z. Zhao and M. Li, *Angew. Chem., Int. Ed.*, 2020, **59**, 20489–20498.

107 S. Jin, D. Zhang, B. Yang, S. Guo, L. Chen and Y. M. Jung, *Analyst*, 2024, **149**, 11–28.

108 I. Deneme, T. A. Yıldız, N. Kayaci and H. Usta, *J. Mater. Chem. C*, 2024, **12**, 3854–3864.

109 S. Huh, J. Park, Y. S. Kim, K. S. Kim, B. H. Hong and J.-M. Nam, *ACS Nano*, 2011, **5**, 9799–9806.

110 X. Yu, H. Cai, W. Zhang, X. Li, N. Pan, Y. Luo, X. Wang and J. G. Hou, *ACS Nano*, 2011, **5**, 952–958.

111 M. Yilmaz, M. Erkartal, M. Ozdemir, U. Sen, H. Usta and G. Demirel, *ACS Appl. Mater. Interfaces*, 2017, **9**, 18199–18206.

112 M. Yilmaz, M. Ozdemir, H. Erdogan, U. Tamer, U. Sen, A. Facchetti, H. Usta and G. Demirel, *Adv. Funct. Mater.*, 2015, **25**, 5669–5676.

113 M. Yilmaz, E. Babur, M. Ozdemir, R. L. Gieseking, Y. Dede, U. Tamer, G. C. Schatz, A. Facchetti, H. Usta and G. Demirel, *Nat. Mater.*, 2017, **16**, 918–924.

114 G. Demirel, R. L. M. Gieseking, R. Ozdemir, S. Kahmann, M. A. Loi, G. C. Schatz, A. Facchetti and H. Usta, *Nat. Commun.*, 2019, **10**, 5502.

115 I. Deneme, G. Liman, A. Can, G. Demirel and H. Usta, *Nat. Commun.*, 2021, **12**, 6119.

116 G.-S. Ryu, Z. Chen, H. Usta, Y.-Y. Noh and A. Facchetti, *MRS Commun.*, 2016, **6**, 47–60.

117 V. Figà, C. Chiappara, F. Ferrante, M. P. Casaletto, F. Principato, S. Cataldo, Z. Chen, H. Usta, A. Facchetti and B. Pignataro, *J. Mater. Chem. C*, 2015, **3**, 5985–5994.

118 K.-S. Wang, Z.-L. Tseng, C.-Y. Liu, T.-Y. Kuan, R.-J. Jeng, M.-C. Yang, Y.-L. Wang and T.-Y. Liu, *Surf. Coat. Technol.*, 2022, **435**, 128251.

119 A. Bhakat and A. Chattopadhyay, *Adv. Opt. Mater.*, 2024, **12**, 2301776.

120 J.-A. Chou, C.-L. Chung, P.-C. Ho, C.-H. Luo, Y.-H. Tsai, C.-K. Wu, C.-W. Kuo, Y.-S. Hsiao, H. Yu and P. Chen, *Front. Chem.*, 2019, **7**, 281.

121 A. Espinha, C. Dore, C. Matricardi, M. I. Alonso, A. R. Goñi and A. Mihi, *Nat. Photonics*, 2018, **12**, 343–348.

122 Y. Lu, Y. Luo, Z. Lin and J. Huang, *Beilstein J. Nanotechnol.*, 2019, **10**, 1270–1279.

123 D. Yan, L. Qiu, M. Xue, Z. Meng and Y. Wang, *Mater. Des.*, 2019, **165**, 107601.

124 Z. Xiong, M. Lin, H. Lin and M. Huang, *Carbohydr. Polym.*, 2018, **189**, 79–86.

125 A. Fularz, S. Almohammed and J. H. Rice, *ACS Sustainable Chem. Eng.*, 2021, **9**, 16808–16819.

126 S. Guo, Y. Park, E. Park, S. Jin, L. Chen and Y. M. Jung, *Angew. Chem., Int. Ed.*, 2023, **62**, e202306709.

127 X.-Y. Zhang, S. Yang, L. Yang, D. Zhang, Y. Sun, Z. Pang, J. Yang and L. Chen, *Chem. Commun.*, 2020, **56**, 2779–2782.

128 Y. Pan, W. Wang, S. Guo, S. Jin, E. Park, Y. Sun, L. Chen and Y. M. Jung, *Chemosensors*, 2021, **9**, 111.

129 Y. Pan, Q. Chu, S. Guo, S. Jin, E. Park, Y. Park, Y. Sun, L. Chen and Y. M. Jung, *Appl. Surf. Sci.*, 2022, **586**, 152863.

130 T. Wang, Y. Lu, L. Xu and Z. J. Chen, *J. Mater. Sci.*, 2022, **57**, 16965–16973.

131 L. Xu, T. Wang, X. Li and Z. Chen, *Chemosensors*, 2022, **10**, 469.

132 S. Almohammed, A. Fularz, M. B. Kanoun, S. Goumri-Said, A. Aljaafari, B. J. Rodriguez and J. H. Rice, *ACS Appl. Mater. Interfaces*, 2022, **14**, 12504–12514.

133 F. Kong, S. Zhang and S. Ding, *J. Appl. Polym. Sci.*, 2023, **141**, e55060.

134 X. Jiang, J. Fu, D. Li, W. Xue and Y. Zhang, *Anal. Lett.*, 2024, **57**, 2455–2468.

135 Z. C. Chen, H. Bin Xu, H. Y. Chen, S. C. Zhu, W. F. Huang, Y. He, M. E. Hafez, R. C. Qian and D. W. Li, *Anal. Chem.*, 2022, **94**, 14280–14289.

136 Z. Yang, C. Ma, J. Gu, Y. Wu, C. Zhu, L. Li, H. Gao, W. Yin, Z. Wang and G. Chen, *Food Chem.*, 2023, **401**, 134078.

137 Y. Xu, C. Wu, N. Chu, J. Yang, Y. Lin and X. Chen, *Sens. Actuators, B*, 2022, **369**, 132361.

138 Q. Wei, L. Shao, H. Pu and D.-W. Sun, *J. Food Meas. Charact.*, 2024, **18**, 2903–2915.

139 Y. Cheng, Y. Ding, J. Chen, W. Xu, W. Wang and S. Xu, *Spectrochim. Acta, Part A*, 2022, **281**, 121644.

140 Z. Yang, C. Ma, J. Gu, Y. Wu, C. Zhu, L. Li, H. Gao, W. Yin, Z. Wang, Y. Zhang, Y. Shang, C. Wang and G. Chen, *Spectrochim. Acta, Part A*, 2022, **267**, 120534.

141 Y. Xie, Q. Li, J. Chen, W. Yue, Z. Xia, M. Zeng, Y. He, Y. Zhao and X. Luo, *Sens. Actuators, B*, 2023, **394**, 134470.

142 X. Feng, Z. Liu, G. Zhang, S. Zhang, S. Huang, Z. He, G. Wei, S. Yang, Y. Zhu, C. Ye, C. Lin, G. Ding and G. Wang, *Energy Environ. Mater.*, 2023, **6**, e12394.

143 H. D. Minh, N. D. Thang, N. T. L. Chi, L. D. Anh, L. N. Long, T. Van Khai, H. C. Khanh, N. D. Khoa and T. H. Minh, *Mater. Res. Express*, 2024, **11**, 025002.

144 S. Guo, E. Park, Y. Byun, H. Chung, S. Jin, Y. Park, L. Chen and Y. M. Jung, *Spectrochim. Acta, Part A*, 2024, **310**, 123892.

145 P. Chettri, V. S. Vendamani, A. Tripathi, M. K. Singh, A. P. Pathak and A. Tiwari, *Appl. Surf. Sci.*, 2017, **406**, 312–318.

146 P. Garg, R. K. Soni and R. Raman, *AIP Conf. Proc.*, 2020, **2220**, 020034.

147 W. Sheng, W. Li, D. Tan, P. Zhang, E. Zhang, E. Sheremet, B. V. K. J. Schmidt, X. Feng, R. D. Rodriguez, R. Jordan and I. Amin, *ACS Appl. Mater. Interfaces*, 2020, **12**, 9797–9805.

148 J. M. González-Domínguez, A. Colusso, L. Litti, A. Ostric, M. Meneghetti and T. Da Ros, *ChemPlusChem*, 2019, **84**, 862–871.

149 D. Liu, X. Chen, Y. Hu, T. Sun, Z. Song, Y. Zheng, Y. Cao, Z. Cai, M. Cao, L. Peng, Y. Huang, L. Du, W. Yang, G. Chen, D. Wei, A. T. S. Wee and D. Wei, *Nat. Commun.*, 2018, **9**, 193.

150 S. Ganesh, K. Venkatakrishnan and B. Tan, *Nat. Commun.*, 2020, **11**, 1135.

151 N. Thuy An, H. Kieu Thi Ta, D. Van Hoang, V. Phung, N. Hoa Thi Tran and B. Thang Phan, *ChemNanoMat*, 2023, **9**, e202200516.

152 H. Ebata, T. Izawa, E. Miyazaki, K. Takimiya, M. Ikeda, H. Kuwabara and T. Yui, *J. Am. Chem. Soc.*, 2007, **129**, 15732–15733.

153 H. Usta, A. Facchetti and T. J. Marks, *Acc. Chem. Res.*, 2011, **44**, 501–510.

154 O. Bubnova, Z. U. Khan, H. Wang, S. Braun, D. R. Evans, M. Fabretto, P. Hojati-Talemi, D. Dagnelund, J.-B. Arlin, Y. H. Geerts, S. Desbief, D. W. Breiby, J. W. Andreasen, R. Lazzaroni, W. M. Chen, I. Zozoulenko, M. Fahlman, P. J. Murphy, M. Berggren and X. Crispin, *Nat. Mater.*, 2014, **13**, 190–194.

155 K. Geng, T. He, R. Liu, S. Dalapati, K. T. Tan, Z. Li, S. Tao, Y. Gong, Q. Jiang and D. Jiang, *Chem. Rev.*, 2020, **120**, 8814–8933.

156 H. Wang, H. Bai, G. Wen, A. Liang and Z. Jiang, *Appl. Mater. Today*, 2022, **27**, 101490.

157 J. Lv, S. Chang, H.-Y. Chen, X.-Y. Zhou, X.-Y. Wang, Z.-C. Chen, B.-B. Chen, R.-C. Qian and D.-W. Li, *Biosens. Bioelectron.*, 2023, **234**, 115325.

158 D. Yao, C. Li, H. Wang, G. Wen, A. Liang and Z. Jiang, *Sens. Actuators, B*, 2020, **319**, 128308.

159 K. S. Novoselov, A. K. Geim, S. V. Morozov, D. Jiang, Y. Zhang, S. V. Dubonos, I. V. Grigorieva and A. A. Firsov, *Science*, 2004, **306**, 666–669.

160 N. Zhang, L. Tong and J. Zhang, *Chem. Mater.*, 2016, **28**, 6426–6435.

161 F. H. L. Koppens, D. E. Chang and F. J. García de Abajo, *Nano Lett.*, 2011, **11**, 3370–3377.

162 A. N. Grigorenko, M. Polini and K. S. Novoselov, *Nat. Photonics*, 2012, **6**, 749–758.

163 L. Xie, X. Ling, Y. Fang, J. Zhang and Z. Liu, *J. Am. Chem. Soc.*, 2009, **131**, 9890–9891.

164 X. Ling, J. Wu, L. Xie and J. Zhang, *J. Phys. Chem. C*, 2013, **117**, 2369–2376.

165 X. Ling and J. Zhang, *Small*, 2010, **6**, 2020–2025.

166 C. Qiu, H. Zhou, H. Yang, M. Chen, Y. Guo and L. Sun, *J. Phys. Chem. C*, 2011, **115**, 10019–10025.

167 X. Ling, J. Wu, W. Xu and J. Zhang, *Small*, 2012, **8**, 1365–1372.

168 H. Xu, L. Xie, H. Zhang and J. Zhang, *ACS Nano*, 2011, **5**, 5338–5344.

169 W. Xu, J. Xiao, Y. Chen, Y. Chen, X. Ling and J. Zhang, *Adv. Mater.*, 2013, **25**, 928–933.

170 Q. Hao, B. Wang, J. A. Bossard, B. Kiraly, Y. Zeng, I.-K. Chiang, L. Jensen, D. H. Werner and T. J. Huang, *J. Phys. Chem. C*, 2012, **116**, 7249–7254.

171 S. Huang, X. Ling, L. Liang, Y. Song, W. Fang, J. Zhang, J. Kong, V. Meunier and M. S. Dresselhaus, *Nano Lett.*, 2015, **15**, 2892–2901.